A snapshot of the earliest stages of normal fault growth

A. Alghuraybi[1*], R. Bell[1], and C. Jackson[1]

[1]*Department of Landscapes and Basin Research Group (LBRG), Earth Science and Engineering, Imperial College, London, UK*

Corresponding author (e-mail: a.alghuraybi19@imperial.ac.uk)

Abstract

Observations of how faults lengthen and accrue displacement during the very earliest stages of their growth are limited, reflecting the fact that the early syn-kinematic sediments that record this growth are often deeply buried and difficult to image with geophysical data. Here, we use borehole and high-quality 3D seismic reflection data from offshore Norway to quantify the lateral propagation (c. 0.38 – 3.4 mm/year) and displacement accumulation (c. 0.0062 – 0.025 mm/year) rates (averaged over 6.2 Myr) for several long (up to 43 km), moderate displacement (up to 155 m), layer-bound faults that we argue provide a unique, essentially 'fossilised' snapshot of the earliest stage of fault growth. We show that lateral propagation rates were up to 300 times faster than displacement rates during the initial ~25% of fault lifespan, suggesting that these faults lengthened much more rapidly than they accrued displacement. Our inference of rapid lengthening is also supported by geometric observations including: (i) low D_{max}-L_{max} (<0.01) scaling relationships, ii) high (>5) length/height aspect ratios, iii) broad, bell-shaped throw-length profiles, and iv) hangingwall depocenters forming during deposition of the first seismically detectable stratigraphic unit spanning the length of the fault. We suggest that the unusually high ratio between lateral propagation rate and displacement rate is likely due to relative immaturity of the studied fault system, an interpretation that supports the ‘constant-length’ fault growth model. Our results highlight the need to document both displacement *and* lateral propagation rates to further our understanding of how faults evolve across various temporal and spatial scales.

1. Introduction

There are currently two end-member fault growth models: (i) the ‘propagating fault model’ and (ii) the ‘constant length model’. The former arises from the apparent scaling relationship between maximum fault displacement (D_{max}) and length (L_{max}) and proposes that faults grow by simultaneously accumulating length and displacement (where D_{max}/L_{max} typically ranges between 1 – 0.01; e.g., Watterson, 1986; Walsh and Watterson, 1988; Cowie and Scholz, 1992; Schlische et al., 1996; Walsh et al., 2003). However, global D_{max}-L_{max} datasets show a high degree of scatter (e.g., Rotevatn et al., 2019), which may reflect, for example, differences in the geological setting within which the studied fault network formed, or uncertainties in measuring the key geometric parameters due to seismic imaging quality or outcrop extent (e.g., Walsh and Watterson, 1988; Gillespie et al., 1992; Kim and Sanderson, 2005). An alternative interpretation is that this variability results from fault maturity, related to the fact that some faults may attain their near-final lengths before accumulating significant displacement (i.e., the constant-length fault model; e.g., Walsh et al., 2002; Meyer et al., 2002; Nicol et al., 2005; Nicol et al., 2016; Childs et al., 2017; Rotevatn et al., 2019, Nicol et al., 2020; Lathrop et al., 2022). Regardless of the precise mode of growth, previous studies have shown that strong mechanical anisotropy in the faulted, horizontally layered host rock can restrict the vertical propagation of faults (e.g., Nicol et al., 1996; Schultz & Fossen, 2002; Soliva et al., 2005; Roche et al., 2013). Faults forming in these rocks may have anomalously high fault aspect ratios (i.e., 3 – 13, compared to 1 – 3 for more typical faults) and strikingly low D-L scaling relationships (i.e., $D_{max}/L < 0.01$) (e.g., Nicol et al., 1996; Schlische et al., 1996; Schultz & Fossen, 2002; Soliva et al., 2005; Roche et al., 2013).

The rate at which faults lengthen and accumulate displacement is a key element of their kinematic history and influences the role they play in controlling the geomorphology, seismic hazard, and resource potential of rift basins (e.g., Walsh et al., 2003). Depending on the period and type of observation, displacement rates vary. For example, over relatively short observational periods (10s years), GPS/geodetic data show that displacement rates can be relatively fast (>10 mm yr^{-1}) and highly variable (e.g., Briole et al., 2000; Wallace et al., 2014) compared to longer-period, typically more stable geological displacement rates (<1 mm yr^{-1}) derived from seismic reflection or field data (e.g., Mouslopoulou et al., 2009; Cowie et al., 2012; Mouslopoulou et al., 2012). This may relate to earthquake clustering events enhancing modern displacement rate estimates over short observational periods (e.g., Cowie et al., 1993; Friedrich et al., 2003; Robinson et al., 2009).

In contrast to displacement, lateral fault tip propagation rates are less frequently reported in fault growth studies, especially over short observational periods. The reason for this varies based on the type of study and dataset used. For example, GPS data can provide some measure of coseismic fault throw (i.e., the vertical component of displacement field derived from GPS location and elevation records) and interseismic creep, but not typically lateral propagation (e.g., Blakeslee & Kattenhorn, 2013). Field studies tend to rely on geomorphic analysis of near-tip drainage patterns (e.g., Jackson et al., 1996) and marine terraces (e.g., Morewood & Roberts 1999), or the stratigraphic architecture of syn-rift strata (e.g., Gawthorpe et al., 1997) to infer lateral propagation rates, although these methods are limited in that they demand well-preserved exposures. These studies show that lateral fault propagation rates can be considerably faster than throw rates (e.g., Morewood & Roberts 1999). However, our current understanding of fault growth, in particular how fluctuations in displacement and lateral propagation rate relate to changes in fault geometry (i.e., aspect ratio), remains poorly constrained. More generally, fault growth models need to quantify both lateral propagation and displacement rates such that they exist within a temporal framework and can thus provide the structural foundation for the tectono-stratigraphic analysis of rift basins at a range of scales (e.g., Walsh et al., 2002; Rotevatn et al., 2019),

Constraining the patterns and rates of fault growth requires the analysis of age-constrained syn-kinematic strata (i.e., strata deposited whilst the fault is active) along the length of faults in 3-dimensions. High-quality 3D seismic reflection data with accompanying biostratigraphy from wells is generally only available from ancient (i.e., inactive), hydrocarbon-bearing rift basins where the syn-rift growth packages are deeply buried and poorly seismically resolved. Alternatively, in active rifts where the syn-rift sediments are shallower (but there is no/limited hydrocarbon interest), the available seismic reflection data are only 2D and often lack age constraints on the syn-rift strata, which could explain the limited observations on earliest stages of normal fault growth.

We here use age-constrained, high-quality 3D seismic reflection and borehole data from the Barents Sea to determine the lateral propagation and displacement rates for several ancient layer-bound faults that we suggest were abandoned before reaching fault maturity. These exceptionally well characterised faults thus provide a snapshot of the earliest stage of fault growth rarely seen in active rifts due to lack of comparable 3D spatial and temporal data coverage.

2. Geological Setting

We have studied a system of low-displacement (< ~150m throw), Middle Jurassic-to-Early Cretaceous normal faults in the SW Barents Sea (Fig. 1), offshore northern Norway where multiple phases of rifting, including one in the Middle Jurassic to Early Cretaceous that formed the faults studied here, shaped the large-scale structure of the region (e.g., Faleide et al., 2008). The tectonic (i.e., non-gravitational) origin of the studied fault system is supported by the fact that they: (i) strike perpendicular to the NNW-SSE extension direction associated with Middle Jurassic to Early Cretaceous rifting; (ii) the basal detachment is not tilted in the direction of fault dip; and (iii) are planar, not listric. The faults developed in Upper Permian/Triassic to Lower Cretaceous clastic rocks deposited on Caledonian crystalline basement (e.g., Doré, 1995). The faulted host rock is characterized by strong mechanical competency contrast between alternating intervals of relatively weak, mudstone-rich strata (i.e., Upper Permian) and mechanically stronger, siltstone- and sandstone-rich layers (i.e., Triassic) (see lithology column in Fig. 2; see also the formation evaluation and gamma-ray log, and lithology well-log in wellbore 7124/4-1S. https://factpages.npd.no/en/wellbore/pageview/exploration/all/6678).

3. Data and Method

We use pre-stack time-migrated 3D seismic reflection data covering c. 533 km^2 and with an estimated vertical resolution of 12.5 – 25 m in the depth range of interest (see Appendix 1). These data allow us to map and describe the map-view and cross-sectional geometry of the studied fault network, and by collecting throw data for nine horizons (seven age-constrained by well data and two of unknown age that mark distinct changes in seismic facies) to show how throw varies across the fault surfaces (Fig. 2). The horizons' ages were constrained by palynological data from wellbore 7124/4-1S (Figs. 1B; 2; see also Appendix 2 for palynological data sample spacing and depth). Two of the age-constrained horizons mark the top and base of the syn-faulting strata, with one occurring within the middle of this unit (see highlighted seismic section in Fig. 2). The age difference between the top and base syn-faulting horizons, therefore, dates the total duration of fault activity. We measure throw values at a 250 m interval on seismic lines trending perpendicular to fault strike and analyse throw values using throw-length (T-x) and throw-depth (T-z) plots (e.g., Cartwright et al., 1995; Jackson et al., 2017). We also produce isochron (time-thickness) maps (to analyse spatial and temporal trends in across-fault thickening; see Schlische, 1995; Gawthorpe et al., 2003; and Jackson & Rotevatn, 2013), throw strike-projections (a plot of throw values across a fault surface; see Walsh and Watterson, 1991 and Alghuraybi et al., 2021), and expansion index (EI) analysis (dividing hangingwall thickness by footwall thickness for corresponding stratal units to constrain the initiation, variability, and cessation of fault activity; see Cartwright et al., 1998; and Jackson & Rotevatn 2013) to further describe the geometry of the fault network and critically assess associated variations in the thickness of syn-kinematic strata (see review by Walsh and Watterson, 1991 and Jackson et al., 2017). We also examine fault growth through time by performing throw backstripping, a technique that involves successively subtracting the throw accumulated on shallower, younger horizons from deeper, older ones (see review by Jackson et al., 2017). All seismic sections are displayed with SEG European Convention (Brown, 2001) with a downward increase and decrease in acoustic impedance represented by a peak (red) and a trough (blue), respectively. Note that all the seismic and wellbore data can be accessed from the Diskos NDR (https://portal.diskos.cgg.com/whereoil-data/) by searching for “Fruholmen 3D” and the well data can be found by searching for “7124/4-1 S”. We use two depth conversion approaches to convert our time measurements from ms TWT (milliseconds two-way time) to depth (Fig. 2). The first method is a simplified layer-cake velocity model that uses velocities derived directly from average sonic log responses from wells that correspond with key seismic intervals (V1; Fig. 2). In the second method we apply a time-depth relationship from our seismic-well-tie (V.2; Fig. 2). The uncertainty in throw arising from using these two different depth-conversion approaches is ±12% (Appendix 3).

We estimate the lateral fault tip propagation rate by taking the fault half-length as measured at the base of the syn-kinematic interval (horizon 4) and dividing it by the time interval to the next age-constrained unit that shows across-fault thickening (i.e., we establish the duration and length of major depocenter development and calculate the lateral bi-directional propagation rate of the fault tips; cf. Childs et al., 2003). Similarly, we calculate the displacement rate by dividing the backstripped displacement (i.e., displacement for the time interval) by the time interval to the next age-constrained horizon (e.g., Nicol et al., 1997; Bell et al., 2009). The displacement value is calculated using measured throw multiplied by fault dip angle (i.e., the inclination of a fault plane relative to a horizontal plane). The fault dip estimation contributes an added uncertainty that should be considered. We provide detailed descriptions of our methods in Figure 3. We then compare these slip rates (lateral propagation and displacement rates) with data from 29 other global datasets from normal faults that formed (or are forming in still-active settings) in various tectonic and depositional settings (see Appendix 4 and 5 for a full list of references).

4. Results

4.1 *Fault network geometry*

The studied fault network consists of 15 Middle Jurassic to Early Cretaceous faults offsetting Early Triassic to Early Cretaceous stratigraphy (Figs. 1B, 2 and 4). Most of these faults tip-out downwards in mudstone-dominated, Permian strata, die-out upwards into Early Cretaceous strata, and are associated with Upper Jurassic growth strata (i.e., they were active in the Middle Jurassic – Early Cretaceous; Fig. 5A). Critically, other stratal units are offset by but do not thicken across the faults, although they thicken regionally, towards the NW, towards the Atlantic margin (Fig. 5C-D). The studied faults are not associated with clear fault bends, abandoned splays or relays (Fig. 4). Most faults are also unusual in that they are: i) notably under-displaced with respect to their lengths (D_{max}/L_{max} = c. 0.001; Fig. 6A); and ii) have anomalously high (up to 25) aspect ratios (Fig. 6 B). Despite having a broad, bell-shaped throw-length profile at the base syn-kinematic level (H4) (Fig. 6C), the fault network shows variable throw-depth profiles with no clear trend representative of all the faults within the network (Fig. 6D.i). However, in detail, we can identify two broad subsets of fault: (I) Subset 1, with throw maxima located at the base of the syn-kinematic interval (H4) and decreasing throw values with depth (Fig. 6D.ii); and (ii) subset 2, which is characterized by two maximum throw values, located at H4 and H9, that are separated by a throw minimum located at H7 (Fig. 6D.iii). Here, we present a detailed geometric analysis of six of the largest and thus well-imaged faults (three from subset 1 and three from subset 2), which are representative of the range of geometric characteristics observed within the fault network.

4.1.1 Observations

Fault 1 (F1; Fig. 7) is approximately 15 km long, with a maximum throw of c. 22 ms (c. 32 m; see depth conversion in Fig. 2) and a maximum displacement of c. 42 m. The longest fault in the network is Fault 8 (F8; Fig. 8), which is c. 43 km long and that has a maximum throw of c. 72 ms (c. 110 m) and a maximum displacement of c. 130 m. Similar to F1 and F8, Fault 10 (F10) strikes E-W, dips to the N and appears to have throw maxima at the base of the syn-kinematic interval (i.e., base Upper Jurassic; Figs. 7, 8 and 9). F10 is c. 10 km long and has a maximum throw and displacement of c. 34 ms (c. 50 m) and c. 66 m, respectively. Faults 1, 8, and 10 are part of subset 1 of the studied fault network and have aspect ratios of c. 13, 25, and 10 (Fig. 6B, D.ii).

The remaining three faults (Faults 6, 11, and 19) are part of subset 2 (Fig. 6D.iii). Like those in subset 1, these faults strike E-W and dip to the N. Fault 6 (F6; Fig. 10) is c. 15 km long, and has a maximum throw of c. 33 ms (c. 50 m) and a maximum displacement of c. 71 m. In contrast, Fault 11 (F11; Fig. 11) is almost twice as long as F6 (c. 31 km long) and has comparable maximum throw and displacement values of c. 55 ms (c. 83 m) and c. 104 m. Like F11, Fault 19 (F19) is also c. 31 km long (Fig. 12). However, F19 has nearly twice as much maximum throw and displacement as F11 (Fig. 12). Both F11 and F19 have aspect ratios of c. 19, whereas F6 has an aspect ratio of c. 11 (Fig. 6B).

The Upper Jurassic strata thicken across all faults within the studied network with EI values >1 for all faults (up to 2.2 and 1.7 for F8 and F11 respectively), defining strike-parallel and elongate depocenters (Fig. 5A). We make two key observations here regarding the fault network. The first is that the lowermost reflections in Upper Jurassic package onlap onto the base syn-kinematic horizon immediately adjacent to the fault tips (H4) (Fig. 13). Although this onlapping relationship is easier to see adjacent to faults associated with thicker Upper Jurassic growth stratigraphy (e.g., F8; Fig. 13iii, iv), it can also be assumed for other faults where the thickness between the lowermost Upper Jurassic package reflections and the base syn-kinematic horizon (H4) is sufficiently small that it is approaching the seismic tuning thickness for our data (c. 14 – 18 m at H4 level). In these cases, instead of the reflections onlapping and truncating in the middle of the fault as they appear in the seismic data, the reflections are likely thinning and onlapping onto H4 closer to the fault tip (Fig. 13i, ii). This interpretation of thinning and onlapping towards the lateral tips of normal faults is supported by field examples from Gulf of Suez, Egypt (see Fig. 4 in Gawthorpe et al.,2003)), where this stratigraphic architecture is interpreted to reflect early establishment of the fault length, consistent with the constant-length model. In some of our subsurface examples, the relatively limited spatial resolution of our seismic reflection dataset limits our ability to interpret the detailed stratigraphic termination and onlap styles readily identified in the field (i.e., we observe only reflection thinning and tuning, and not discrete onlap; e.g., Bakke et al., 2013). The second key observation is that Upper Jurassic growth strata clearly thicken across the faults just inboard of their fault tips (Fig. 14i). In fact, we observe the development of strike-parallel depocenters and their associated across-fault thickening of growth strata in the lowermost seismically resolvable unit (H3-H4) (Fig. 14i.A). For instance, we can see that the location of the fault tips and formation of the strike-parallel depocenters are corresponding with the base syn-kinematic horizon having EI values of >1 and the highest backstripped throw along-strike of both F8 and F11 (Fig. 14ii-v).

4.1.2 Interpretation

Growth strata show that the studied faults were active from 163.5 – 132.6 Ma (i.e., in the Middle Jurassic – Early Cretaceous (H4-H1); Figs. 5A, 14) for both subsets 1 and 2. The presence of multiple throw maxima along the same stratigraphic level on some of the subset 1 faults (e.g., F1 and F8; Figs. 7, 8) provides geometric evidence that they grew by lateral segment linkage (e.g., Cartwright et al., 1995). However, the lack of obvious bends, breached relays, or abandoned splays suggests that the precursor segments did not overlap, and may have formed part of a single, kinematically linked structure from their inception (e.g., Childs et al., 2017). This interpretation is supported by the fact that the across-fault thickening we observe occurs along almost the entire –strike-length of the faults and is associated with onlap of the lowermost syn-kinematic onto pre-kinematic strata immediately inboard of the lateral fault tips (Fig. 13). In contrast, based on the observation that subset 2 faults have multiple throw maxima along different stratigraphic intervals (H4, H9) that are separated by a throw minimum that occurs at the same stratigraphic interval for all faults (H7), we suggest the presence of an intraformational detachment layer in addition to the lower, regional detachment onto which all faults terminate (Fig. 6D). Therefore, subset 2 faults likely nucleated at different stratigraphic levels (H4, H9) and vertically linked at a later stage during the faults' lives (Fig. 15; e.g., Nicol et al., 1996; Soliva et al., 2005; Roche et al., 2013). By analysing the map-view locations of where vertical linkage occurred, we do not see any strong trends that highlight areas of favourable vertical linkage (Fig. 15). Instead, the lack of any clear trends suggests that the strong mechanical anisotropy observed from the wellbore data (Fig. 2) might also vary laterally across the study area.

4.2 Fault growth rates

In addition to the geometric properties of the fault network, we also assess the kinematic properties of these faults, to gain insight into normal fault growth patterns by analysing displacement and lateral propagation rates of the fault network. We then compare and contextualise these slip rates with data from 29 other global datasets from normal faults that formed (or are forming in still-active settings) in various tectonic and depositional settings (Fig. 16A). Our compiled dataset is not intended to be exhaustive; it simply allows us to compare our faults with some global examples of rates determined across different observational periods.

We calculate the displacement and lateral propagation rates using the time between the two dated horizons at the base (H4) and middle (H2) of the syn-kinematic package (Fig. 2). This results in a period of 6.2 Myrs, which we argue should be considered as an upper limit of the duration of fault activity. In fact, our detailed geometric analysis showed that the strike-parallel depocenters formed in the hangingwalls of the studied faults over a shorter period than the time between the two horizons defining the top and middle of the syn-kinematic package (<6.2 Myr; Fig. 14i), however we do not have age-control on horizons between H4 and H2. In the absence of higher resolution age constraints, we speculate that the similarity in seismic facies characteristics in the syn-kinematic interval could indicate similar lithology and potentially a similar sedimentation rate within the syn-kinematic interval (c. 7 m/Myr for the 6.2 Myr period based on wellbore data). If the sediment accumulation rate was constant, then we might infer the duration of the earliest stage of fault development (i.e., the time duration between horizon H4 and H3) to be c. 3.1 Myrs instead of 6.2 Myr, based on the observation that the thickness of the earliest seismically resolvable depocenter is c. 50% of the total thickness of the 6.2 Myr syn-kinematic package (Figs. 2, 13, and 14). Therefore, the values shown in Fig.

16 should be regarded as lower estimates of displacement and lateral propagation rates of the studied fault network, given we show rates calculated using a time period of 6.2 Myr.

Our studied faults show relatively low displacement rates (i.e., c. 0.0062 – 0.025 mm/year averaged over a 6.2 Myr duration of fault activity and c. 0.012 – 0.050 mm/year averaged over a 3.1 Myr period) compared to the global dataset (Fig. 16A). These displacement rates are comparable to those measured over similar time scales (i.e., >10^7 years; Fig. 16A) in the North Sea (Nicol et al., 1997; Bell et al., 2014), the Timor Sea (Meyer et al., 2002), and the Basin & Range and Taranaki Rift (Mouslopoulou et al., 2009), or for faults with similar trace lengths (>10^4 km; Fig. 16B; Lathrop et al., 2021) averaged over longer time scales. In contrast, for faults active for a comparable time period, our studied fault network shows higher lateral propagation rates (i.e., c. 0.38 – 3.4 mm/year and 0.76 – 6.9 mm/year based on fault ages of 6.2 and 3.1 Myr respectively), being approximately an order of magnitude faster (Fig. 16A). However, faults active for shorter durations (i.e., 10^5 – 10^6 years) appear to have faster lateral propagation rates (i.e., approximately an order to magnitude higher) compared to our studied fault network (Fig. 16A).

Depending on the growth paths these faults took (i.e., constant length model vs. propagating fault model), a relationship should emerge between the rate of lateral propagation, fault displacement rate, and fault maturity. Specifically, if the faults grew in accordance with the propagating fault model, the ratio between lateral propagation and displacement rate will be closer to 1. However, if the faults established their lengths before accruing significant displacement, then the ratio between lateral propagation and displacement would be >1, especially during the early stages of fault development (i.e., initial 20 – 30% of fault lifespan; e.g., Walsh et al., 2002; Meyer et al., 2002; Nicol et al., 2005; Nicol et al., 2016; Childs et al., 2017; Rotevatn et al., 2019, Nicol et al., 2020; Lathrop et al., 2022). We observe that independent of fault length and whether the duration of faulting is estimated to be 6.2 or 3.1 Myr, the studied faults propagated laterally much more rapidly (i.e., c. 300 - 20 times faster) than they accumulated displacement (Fig. 16C). This value is 2-3 orders of magnitude higher than for other seismically imaged faults of similar length (Fig. 16C; e.g., Bell et al., 2009; Lathrop et al., 2021).

5. DISCUSSION

The studied fault network is characterized by faults having i) low (c. 0.001) D_{max}-L_{max} scaling relationships (Fig. 6A), ii) high (>5) length/height aspect ratios (Fig. 6B), iii) a broad, bell-shaped throw-length profile at the base syn-kinematic level (H4; Fig. 6C), iv) hangingwall depocenters forming at first detectable unit above the base syn-kinematic horizon (H4; Fig 14i), and v) onlap of the lowermost syn-kinematic strata onto pre-kinematic strata immediately inboard of the lateral fault tips (Fig. 13). These geometric observations suggest that the studied network captures faults during their very earliest stage of development when they were growing in accordance with the constant-length model. Along with the geometric properties of the fault network, our kinematic analysis shows that these faults propagated laterally much faster than they accumulated displacement (Fig. 16C). Combining the geometric and kinematic observations indicates that the studied faults rapidly lengthened and reached their near-final lengths but did not have a chance to accumulate significant additional displacement (i.e., faults are *geometrically* immature) before becoming inactive (e.g., Walsh et al., 2002; Meyer et al., 2002; Nicol et al., 2005; Nicol et al., 2016; Childs et al., 2017). Why the faults became inactive is unknown, although we suspect this is related to strain localization on to the nearby, very large (c. 2 km displacement), basement-rooted, Troms-Finnmark Fault Complex (TFFC), which continued to be active until the Eocene (e.g., Alghuraybi et al., 2021). It could be argued that the presence of a weak mudstone at the bottom of the faulted interval inhibits downward propagation and limits the accumulation of additional displacement, leading to high aspect ratios (Schultz & Fossen, 2002). However, we maintain that the early formation of strike-parallel hangingwall depocenters (Fig. 14i) and the observed onlap relationships (Fig 13), combined with the other geometric properties of the fault network, favour the interpretation of the rapid propagation rate being a function of early-stage faulting rather than vertical restriction alone.

The highest aspect ratio ever reported for a natural normal fault that we are aware of is 12 (Nicol et al., 1996; Soliva et al., 2005; Roche et al., 2013); this is significantly lower than the highest aspect ratio we observe here (c. 25). In fact, five of the studied faults have aspect ratios >>13 (Fig. 6B). Numerical models, motivated by observations from meter-scale fault networks in layered carbonate rocks, show that aspect ratios can vary through time, increasing when the faults interact with layers that restrict their onwards vertical propagation, before decreasing again when they are able to breach those layers (e.g., Soliva et al., 2005; Roche et al., 2013). Our study suggests that this process may occur at substantially larger scales than previous reported, meaning aspect ratio variability is a fundamental aspect of fault growth across scales in mechanically layered rocks.

Our slip rate data compilation builds on previous works (e.g., Nicol et al., 2005; Mouslopoulou et al., 2009; Nicol et al., 2020) and includes lateral propagation and displacement rate data measured over a range of temporal scales using different methods (geodetic, GPS, field observations, seismic refraction, and reflection data). By compiling the database, we note that lateral propagation rates are often not reported or less frequently documented compared to displacement rates. Based on this we propose to document, where possible, both displacement *and* lateral propagation rates. By doing so, we can further our understanding of how faults evolve across various temporal and spatial scales.

6. CONCLUSION

We study a normal fault network from SW Barents Sea, offshore Norway using high-quality 3D seismic reflection and borehole data. The fault network consists of 15 Middle Jurassic to Early Cretaceous normal faults that offset a Late Triassic to Early Cretaceous stratigraphy and are associated with Upper Jurassic growth strata. These faults are characterised by i) anomalously low (c. 0.001) D_{max}-L_{max} scaling relationships, ii) unusually high (up to 25) aspect ratios, iii) broad, bell-shaped throw-length profile at the base syn-kinematic level, and iv) hangingwall depocenters forming within the first detectable unit above the base syn-kinematic horizon. By quantifying the faults' lateral propagation (c. 0.76 – 6.9 mm/year) and displacement accumulation (c. 0.012 – 0.050 mm/year) rates, we show that these faults developed up to 300 times faster than accumulated displacement. Based on the geometric properties of these faults and their rapid lateral propagation relative to displacement accumulation rates, we propose that these faults represent a "fossilised" snapshot of the earliest stages of normal fault growth, where the faults reached their near-final lengths before accumulating any significant displacement resulting in *geometrically* immature faults.

Acknowledgements

The results presented here are part of AA's PhD research at Imperial College London, funded by Saudi Aramco. We thank the Norwegian Petroleum Directorate the publicly data (https://portal.diskos.cgg.com/whereoil-data/) and Schlumberger for Petrel software. We also thank Andy Nicol for the constructive feedback on a previous version of this work.

Author contributions

AA: data analysis, investigation, conceptualisation, writing – original draft; RB: conceptualisation, supervision, writing – review & editing; CJ: conceptualisation, supervision, writing – review & editing

Data availability

The seismic and wellbore data are openly available in the Norwegian national data repository for petroleum data at https://portal.diskos.cgg.com/whereoil-data/. The slip rate data compilation and depth conversion data are available at https://doi.org/10.6084/m9.figshare.21681107.v1

FIGURE CAPTIONS

Figure 1: (A) Map showing study area location and regional geology of SW Barents Sea. The map is modified after information found in the Norwegian Petroleum Directorate fact page http://www.npd.no/en/. **(B)** A time-structure map of the base syn-kinematic unit (H4) with a white-dashed line indicating the location of the seismic section in Fig. 2. The location of wellbore 7124/4-1S is noted by a green star while the study area is outlined by the blue border.

Figure 2: A representative seismic cross-section highlighting the geometry of the studied faults and horizon's age and lithology as constrained by wellbore 7124/4-1S. The section also includes Gamma Ray (GR) log data, modelled interval velocity using simplified geological model (V.1) and calculated pseudo interval velocity using estimated time-depth relationship from seismic well tie (V.2).

Figure 3: Detailed description of the methodology we use to calculate fault throw, displacement, displacement accumulation rate (Displacement Rate), lateral propagation rate (Lateral Propagation Rate), and fault length / height aspect ratio (Aspect Ratio).

Figure 4: Time-structure maps for the Early Cretaceous (H1), Middle Jurassic (H4), Middle Triassic (H6) and Lower Triassic (H8) horizons. The location of the fault network and names of the studied faults are annotated on (B).

Figure 5: Isochron (time-thickness) maps for the L. Cretaceous to M. Jurassic **(A)**, L. Jurassic to U. Triassic **(B)**, M. Triassic **(C)** and L. Triassic **(D)**. These isochrons show the clear across-fault thickening in the Early Cretaceous to Middle Jurassic and general constant thickness nature of the other time intervals.

Figure 6: A summary of the geometric properties of the fault network showing **(A)** D_{max}-L_{max} plot from a global database of normal faults (modified after Lathrop et al., 2022). Data for studied fault network are shown in yellow while literature data are showing in blue (active faults) and grey (inactive faults). **(B)** Aspect ratio (length/height) distribution of the studied fault network with dashed-horizontal lines showing average aspect ratios of “blind isolated normal faults in layered sequences” (yellow), maximum aspect ratio of restricted faults (red) (Nicol et al., 1996) and maximum aspect ratio for faults cutting formations with strong mechanical contrast (green) (Roche et al., 2013). **(C)** Normalized throw-length plot for the studied faults (grey) at the base syn-kinematic level (H4) with an average profile of the fault network shown in yellow. **(D)** Normalized throw-depth profiles for the studied faults showing the basal detachment layer **(i)**. The fault network can be divided into two subsets with subset 1 including faults F1, F5, F8, F10, F17 and F21 **(ii)** showing a single throw maximum at the H4 level while subset 2 (F2, F3, F6, F9, F11, F13, F15, F16, and F19) **(iii)** shows the presence of a potential intra-stratal detachment layer that separates two throw maxima denoting potential vertical (i.e., dip) linkage. The Expansion Index (EI) values of H4, H6, H7, H8 and H9 are shown to the side of the normalized throw-depth plots.

Figure 7: A detailed overview of Fault 1 (F1) showing **(A)** a strike-parallel seismic section, **(B)** a strike-perpendicular (dip) seismic section, **(C)** strike-projected throw distribution along the fault surface, **(D)** A time-structure map of the base syn-kinematic horizons (H4) denoting the fault map location and the location of sections **(A)** and **(B)**. **(E)** Expansion Index (EI) values showing potential across fault thickening (i.e., syn-kinematic growth) at the H4 level.

Figure 8: A detailed overview of Fault 8 (F8) showing **(A)** a strike-parallel seismic section, **(B)** a strike-perpendicular (dip) seismic section, **(C)** strike-projected throw distribution along the fault surface, **(D)** A time-structure map of the base syn-kinematic horizons (H4) denoting the fault map location and the location of sections **(A)** and **(B)**. **(E)** Expansion Index (EI) values showing potential across fault thickening (i.e., syn-kinematic growth) at the H4 level.

Figure 9: A detailed overview of Fault 10 (F10) showing **(A)** a strike-parallel seismic section, **(B)** a strike-perpendicular (dip) seismic section, **(C)** strike-projected throw distribution along the fault surface, **(D)** A time-structure map of the base syn-kinematic horizons (H4) denoting the fault map location and the location of sections **(A)** and **(B)**. **(E)** Expansion Index (EI) values showing potential across fault thickening (i.e., syn-kinematic growth) at the H4 level.

Figure 10: A detailed overview of Fault 6 (F6) showing **(A)** a strike-parallel seismic section, **(B)** a strike-perpendicular (dip) seismic section, **(C)** strike-projected throw distribution along the fault surface, **(D)** A time-structure map of the base syn-kinematic horizons (H4) denoting the fault map location and the location of sections **(A)** and **(B)**. **(E)** Expansion Index (EI) values showing potential across fault thickening (i.e., syn-kinematic growth) at the H4 level.

Figure 11: A detailed overview of Fault 11 (F11) showing **(A)** a strike-parallel seismic section, **(B)** a strike-perpendicular (dip) seismic section, **(C)** strike-projected throw distribution along the fault surface, **(D)** A time-structure map of the base syn-kinematic horizons (H4) denoting the fault map location and the location of sections **(A)** and **(B)**. **(E)** Expansion Index (EI) values showing potential across fault thickening (i.e., syn-kinematic growth) at the H4 level.

Figure 12: A detailed overview of Fault 19 (F19) showing **(A)** a strike-parallel seismic section, **(B)** a strike-perpendicular (dip) seismic section, **(C)** strike-projected throw distribution along the fault surface, **(D)** A time-structure map of the base syn-kinematic horizons (H4) denoting the fault map location and the location of sections **(A)** and **(B)**. **(E)** Expansion Index (EI) values showing potential across fault thickening (i.e., syn-kinematic growth) at the H4 level.

Figure 13: Un-interpreted and interpreted strike-parallel sections along faults F1 **(i, ii)** and F8 **(iii, iv)** showing the lowermost reflections in Upper Jurassic package onlapping onto the base syn-kinematic horizon immediately adjacent to the fault tips (blue arrow). **(ii.A, ii.B)** A schematic representation of two possible interpretations along strike of F1 where the blue arrow shows the onlap and truncation scenario before the fault tip and the green arrow shows the onlap and thinning case towards the fault tip. The two interpretations **(ii.A, ii.B)** illustrate the implication of seismic tuning on the observations of the intraformational architecture.

Figure 14: **(i)** Isochron (time-thickness) maps for sub-units of the syn-kinematic interval (Middle Jurassic to Early Cretaceous) showing across-fault thickening in the smallest resolvable interval. **(ii)** and **(iii)** Expansion Index (EI) values along strike of faults 8 (F8) and 11 (F11) showing values >1 along at the H4 level along strike of the entire fault surface. **(iv)** and **(v)** backstripped throw vs. length profiles for F8 and F11 highlighting maximum throw occurring at H4 level and showing the location of the fault tips.

Figure 15: Time-structure map of the base syn-kinematic level (H4) showing the studied fault network. Faults coloured in black are the ones that show no sign of vertical linkage while faults coloured in white indicate faults that exhibit vertical linkage. The blue fill-colour within the white faults highlights the map location of the inferred vertical linkage. Strike-projections A-F show the fault examples discussed in-text with hangingwall and footwall throw traces indicated by solid and dashed lines for horizons H4, H7, and H8. The strike-projections illustrate the lack of any throw maxima below H7 for subset 1 faults (F1, F8, F10) and the presence of an intraformational detachment layer at H7 that separates different throw maxima above and below the detachment for subset 2 faults (F6, F11, F13).

Figure 16: **(A)** Slip rate data across various timescales for the studied fault network (displacement rates in light blue and lateral propagation rates in light green) and literature data (displacement rates in dark blue and lateral propagation rates in red). The shape of the literature data points relates to their type/origin. Each literature study is represented by two points marking the maximum and minimum reported rates in the study and the line connecting the two points captures the range of reported data by each study. Another version of this plot is provided in Appendix 4 where each literature study is clearly indicated, and the literature data is provided in Appendix 5. **(B)** Slip rate data (displacement rates) across various fault lengths. **(C)** A plot of the ratio of lateral propagation and displacement rates for the studied faults (dark blue), data from Bell et al. (2009) (grey circles) and Lathrop et al. (2021) (grey crosses). The plot shows that the studied fault network has a ratio that is 2-3 orders of magnitude higher than other seismically imaged faults of similar length. Please note that we plot the maximum and minimum slip rate data from each study and connect those two points with a line to represent the full range of rates reported (Fig. 16A).

References

Alghuraybi, A., Bell, R. E., & Jackson, C. A. L. (2022). The geometric and temporal evolution of fault-related folds constrain normal fault growth patterns, Barents Sea, offshore Norway. *Basin Research*, *34*(2), 618-639. https://doi.org/10.1111/bre.12633

Bakke, K., Kane, I. A., Martinsen, O. J., Petersen, S. A., Johansen, T. A., Hustoft, S., Jacobsen, F. H., & Groth, A. (2013). Seismic modeling in the analysis of deep-water sandstone termination stylesGeohorizon. *AAPG bulletin*, *97*(9), 1395-1419. https://doi.org/10.1306/03041312069

Bell, R. E., McNeill, L. C., Bull, J. M., Henstock, T. J., Collier, R. L., & Leeder, M. R. (2009). Fault architecture, basin structure and evolution of the Gulf of Corinth Rift, central Greece. *Basin Research*, *21*(6), 824-855. https://doi.org/10.1111/j.1365-2117.2009.00401.x

Bell, R. E., Jackson, C. A. L., Whipp, P. S., & Clements, B. (2014). Strain migration during multiphase extension: Observations from the northern North Sea. *Tectonics*, *33*(10), 1936-1963. https://doi.org/10.1002/2014TC003551

Blakeslee, M. W., & Kattenhorn, S. A. (2013). Revised earthquake hazard of the Hat Creek fault, northern California: A case example of a normal fault dissecting variable-age basaltic lavas. *Geosphere*, *9*(5), 1397-1409. https://doi.org/10.1130/GES00910.1

Briole, P., Rigo, A., Lyon-Caen, H., Ruegg, J. C., Papazissi, K., Mitsakaki, C., Balodimou, A., Veis, G., Hatzfeld, D., & Deschamps, A. (2000). Active deformation of the Corinth rift, Greece: results from repeated Global Positioning System surveys between 1990 and 1995. *Journal of Geophysical Research: Solid Earth*, *105*(B11), 25605-25625. https://doi.org/10.1029/2000JB900148

Brown, A. R. (2001). Color in seismic display. *The Leading Edge*, *20*(5), 549-549. https://doi.org/10.1190/1.1438992.

Cartwright, J. A., Trudgill, B. D., & Mansfield, C. S. (1995). Fault growth by segment linkage: an explanation for scatter in maximum displacement and trace length data from the Canyonlands Grabens of SE Utah. *Journal of structural Geology*, *17*(9), 1319-1326. https://doi.org/10.1016/0191-8141(95)00033-A

Cartwright, J., Bouroullec, R., James, D., & Johnson, H. (1998). Polycyclic motion history of some Gulf Coast growth faults from high-resolution displacement analysis. *Geology*, *26*(9), 819-822. https://doi.org/10.1130/0091-7613(1998)026<0819:PMHOSG>2.3.CO;2

Childs, C., Nicol, A., Walsh, J. J., & Watterson, J. (2003). The growth and propagation of synsedimentary faults. *Journal of Structural geology*, *25*(4), 633-648. https://doi.org/10.1016/S0191-8141(02)00054-8

Childs, C., Holdsworth, R. E., Jackson, C. A. L., Manzocchi, T., Walsh, J. J., & Yielding, G. (2017). Introduction to the geometry and growth of normal faults. *Geological Society, London, Special Publications, 439*(1), 1-9. https://doi.org/10.1144/SP439.24

Cowie, P. A., & Scholz, C. H. (1992). Displacement-length scaling relationship for faults: data synthesis and discussion. *Journal of Structural Geology*, *14*(10), 1149-1156. https://doi.org/10.1016/0191-8141(92)90066-6

Cowie, P. A., Vanneste, C., & Sornette, D. (1993). Statistical physics model for the spatiotemporal evolution of faults. *Journal of Geophysical Research: Solid Earth*, *98*(B12), 21809-21821. https://doi.org/10.1029/93JB02223

Cowie, P. A., Roberts, G. P., Bull, J. M., & Visini, F. (2012). Relationships between fault geometry, slip rate variability and earthquake recurrence in extensional settings. *Geophysical Journal International*, *189*(1), 143-160. https://doi.org/10.1111/j.1365-246X.2012.05378.x

Doré, A. G. (1995). Barents Sea geology, petroleum resources and commercial potential. *Arctic*, 207-221. https://www.jstor.org/stable/40511656

Faleide, J. I., Tsikalas, F., Breivik, A. J., Mjelde, R., Ritzmann, O., Engen, Ø., Wilson, J., & Eldholm, O. (2008). Structure and evolution of the continental margin off Norway and the Barents Sea. *Episodes Journal of International Geoscience*, *31*(1), 82-91. https://doi.org/10.18814/epiiugs/2008/v31i1/012

Friedrich, A. M., Wernicke, B. P., Niemi, N. A., Bennett, R. A., & Davis, J. L. (2003). Comparison of geodetic and geologic data from the Wasatch region, Utah, and implications for the spectral character of Earth deformation at periods of 10 to 10 million years. *Journal of Geophysical Research: Solid Earth*, *108*(B4). https://doi.org/10.1029/2001JB000682

Gawthorpe, R. L., Jackson, C. A. L., Young, M. J., Sharp, I. R., Moustafa, A. R., & Leppard, C. W. (2003). Normal fault growth, displacement localisation and the evolution of normal fault populations: the Hammam Faraun fault block, Suez rift, Egypt. *Journal of Structural Geology*, *25*(6), 883-895. https://doi.org/10.1016/S0191-8141(02)00088-3

Gawthorpe, R. L., Sharp, I., Underhill, J. R., & Gupta, S. (1997). Linked sequence stratigraphic and structural evolution of propagating normal faults. *Geology*, *25*(9), 795-798. https://doi.org/10.1130/0091-7613(1997)025<0795:LSSASE>2.3.CO;2

Gillespie, P. A., Walsh, J. T., & Watterson, J. (1992). Limitations of dimension and displacement data from single faults and the consequences for data analysis and interpretation. *Journal of Structural Geology*, *14*(10), 1157-1172. https://doi.org/10.1016/0191-8141(92)90067-7

Jackson, J., Norris, R., & Youngson, J. (1996). The structural evolution of active fault and fold systems in central Otago, New Zealand: evidence revealed by drainage patterns. *Journal of Structural Geology*, *18*(2-3), 217-234. https://doi.org/10.1016/S0191-8141(96)80046-0

Jackson, C. A. L., & Rotevatn, A. (2013). 3D seismic analysis of the structure and evolution of a salt-influenced normal fault zone: a test of competing fault growth models. *Journal of Structural Geology*, *54*, 215-234. https://doi.org/10.1016/j.jsg.2013.06.012

Jackson, C. A. L., Bell, R. E., Rotevatn, A., & Tvedt, A. B. (2017). Techniques to determine the kinematics of synsedimentary normal faults and implications for fault growth models. *Geological Society, London, Special Publications*, *439*(1), 187-217. https://doi.org/10.1144/SP439.22

Kim, Y. S., & Sanderson, D. J. (2005). The relationship between displacement and length of faults: a review. *Earth-Science Reviews*, *68*(3-4), 317-334. https://doi.org/10.1016/j.earscirev.2004.06.003

Lathrop, B. A., Jackson, C. A. L., Bell, R. E., & Rotevatn, A. (2021). Normal fault kinematics and the role of lateral tip retreat: An example from offshore NW Australia. *Tectonics*, *40*(5), e2020TC006631. https://doi.org/10.1029/2020TC006631

Lathrop, B., Jackson, C., Bell, R. E., & Rotevatn, A. (2022). Displacement/length scaling relationships for normal faults; a review, critique, and revised compilation. https://doi.org/10.31223/X58S7G

Meyer, V., Nicol, A., Childs, C., Walsh, J. J., & Watterson, J. (2002). Progressive localisation of strain during the evolution of a normal fault population. *Journal of Structural Geology*, *24*(8), 1215-1231. https://doi.org/10.1016/S0191-8141(01)00104-3

Morewood, N. C., & Roberts, G. P. (1999). Lateral propagation of the surface trace of the South Alkyonides normal fault segment, central Greece: its impact on models of fault growth and displacement–length relationships. *Journal of Structural Geology*, *21*(6), 635-652. https://doi.org/10.1016/S0191-8141(99)00049-8

Mouslopoulou, V., Walsh, J. J., & Nicol, A. (2009). Fault displacement rates on a range of timescales. *Earth and Planetary Science Letters*, *278*(3-4), 186-197. https://doi.org/10.1016/j.epsl.2008.11.031

Mouslopoulou, V., Nicol, A., Walsh, J. J., Begg, J. G., Townsend, D. B., & Hristopulos, D. T. (2012). Fault-slip accumulation in an active rift over thousands to millions of years and the importance of paleoearthquake sampling. *Journal of Structural Geology*, *36*, 71-80. https://doi.org/10.1016/j.jsg.2011.11.010

Nicol, A., Watterson, J., Walsh, J. J., & Childs, C. (1996). The shapes, major axis orientations and displacement patterns of fault surfaces. *Journal of Structural Geology*, *18*(2-3), 235-248. https://doi.org/10.1016/S0191-8141(96)80047-2

Nicol, A., Walsh, J. J., Watterson, J., & Underhill, J. R. (1997). Displacement rates of normal faults. *Nature*, *390*(6656), 157-159. https://doi.org/10.1038/36548

Nicol, A., Walsh, J. J., Manzocchi, T., & Morewood, N. (2005). Displacement rates and average earthquake recurrence intervals on normal faults. *Journal of Structural Geology*, *27*(3), 541-551. https://doi.org/10.1016/j.jsg.2004.10.009

Nicol, A., Robinson, R., Van Dissen, R. J., & Harvison, A. (2016). Variability of recurrence interval and single-event slip for surface-rupturing earthquakes in New Zealand. *New Zealand Journal of Geology and Geophysics*, *59*(1), 97-116. https://doi.org/10.1080/00288306.2015.1127822

Nicol, A., Mouslopoulou, V., Begg, J., & Oncken, O. (2020). Displacement accumulation and sampling of paleoearthquakes on active normal faults of Crete in the eastern Mediterranean. *Geochemistry, Geophysics, Geosystems*, *21*(11), e2020GC009265. https://doi.org/10.1029/2020GC009265

Robinson, R., Nicol, A., Walsh, J. J., & Villamor, P. (2009). Features of earthquake occurrence in a complex normal fault network: Results from a synthetic seismicity model of the Taupo Rift, New Zealand. *Journal of Geophysical Research: Solid Earth*, *114*(B12). https://doi.org/10.1029/2008JB006231

Roche, V., Homberg, C., & Rocher, M. (2013). Fault nucleation, restriction, and aspect ratio in layered sections: Quantification of the strength and stiffness roles using numerical modeling. *Journal of Geophysical Research: Solid Earth*, *118*(8), 4446-4460. https://doi.org/10.1002/jgrb.50279

Rotevatn, A., Jackson, C. A. L., Tvedt, A. B., Bell, R. E., & Blækkan, I. (2019). How do normal faults grow?. *Journal of Structural Geology*, *125*, 174-184. https://doi.org/10.1016/j.jsg.2018.08.005

Schlische, R. W. (1995). Geometry and origin of fault-related folds in extensional settings. *AAPG bulletin*, *79*(11), 1661-1678. https://doi.org/10.1306/7834DE4A-1721-11D7-8645000102C1865D

Schlische, R. W., Young, S. S., Ackermann, R. V., & Gupta, A. (1996). Geometry and scaling relations of a population of very small rift-related normal faults. *Geology*, *24*(8), 683-686. https://doi.org/10.1130/0091-7613(1996)024%3C0683:GASROA%3E2.3.CO;2

Soliva, R., & Benedicto, A. (2005). Geometry, scaling relations and spacing of vertically restricted normal faults. *Journal of Structural Geology*, *27*(2), 317-325. https://doi.org/10.1016/j.jsg.2004.08.010

Wallace, L. M., Ellis, S., Little, T., Tregoning, P., Palmer, N., Rosa, R., Stanaway, R., Oa, J., Nidkombu, E., & Kwazi, J. (2014). Continental breakup and UHP rock exhumation in action: GPS results from the W oodlark R ift, P apua N ew G uinea. *Geochemistry, Geophysics, Geosystems*, *15*(11), 4267-4290. https://doi.org/10.1002/2014GC005458

Walsh, J. J., & Watterson, J. (1988). Analysis of the relationship between displacements and dimensions of faults. *Journal of Structural geology*, *10*(3), 239-247. https://doi.org/10.1016/0191-8141(88)90057-0

Walsh, J. J., & Watterson, J. (1991). Geometric and kinematic coherence and scale effects in normal fault systems. *Geological Society, London, Special Publications*, *56*(1), 193-203. https://doi.org/10.1144/GSL.SP.1991.056.01.13

Walsh, J. J., Bailey, W. R., Childs, C., Nicol, A., & Bonson, C. G. (2003). Formation of segmented normal faults: a 3-D perspective. *Journal of Structural Geology*, *25*(8), 1251-1262. https://doi.org/10.1016/S0191-8141(02)00161-X

Walsh, J. J., Nicol, A., & Childs, C. (2002). An alternative model for the growth of faults. *Journal of Structural Geology*, *24*(11), 1669-1675. https://doi.org/10.1016/S0191-8141(01)00165-1

Watterson, J. (1986). Fault dimensions, displacements and growth. *Pure and Applied Geophysics*, *124*(1), 365-373. https://doi.org/10.1007/BF00875732

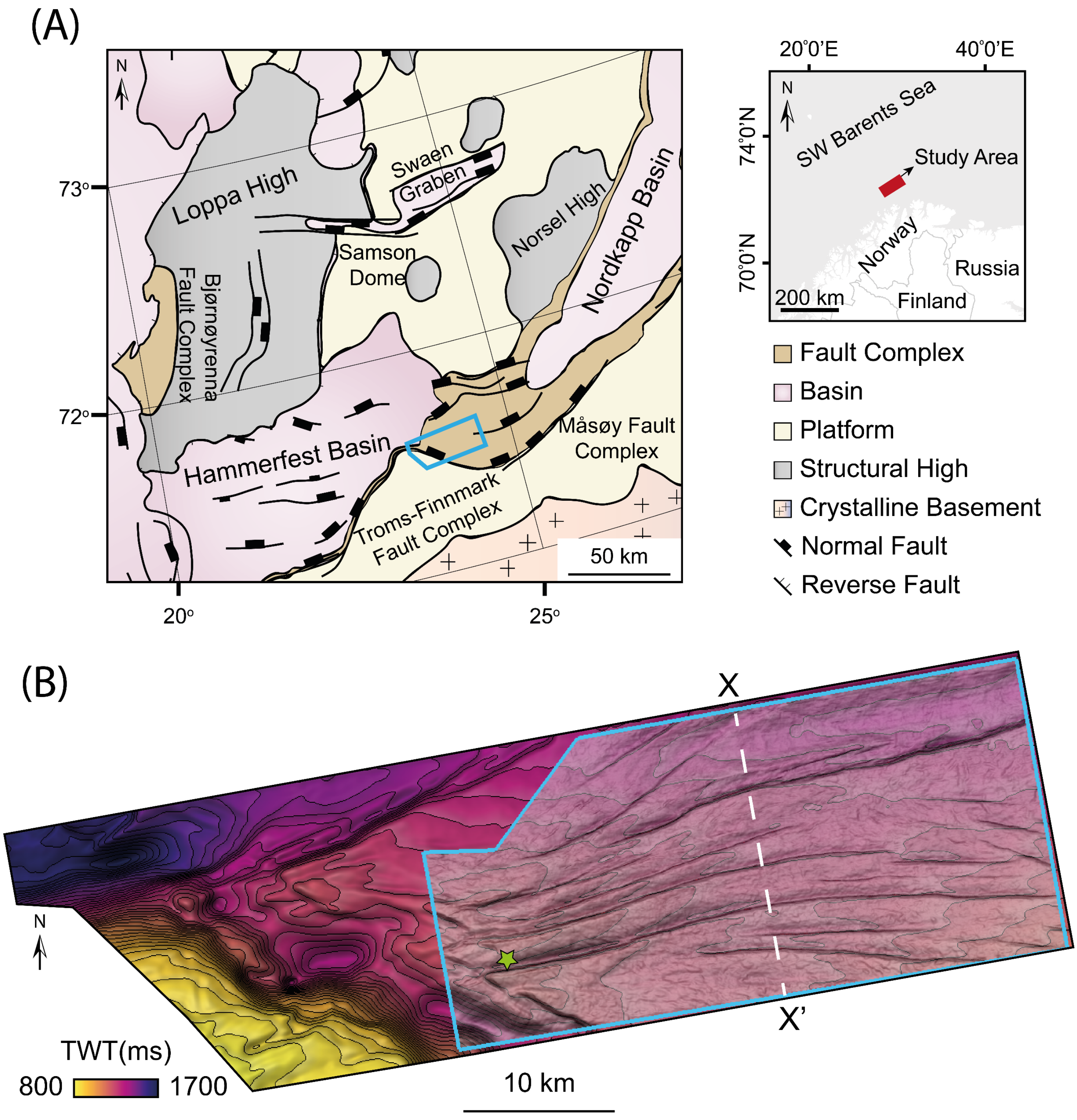

Figure 1: (A) Map showing study area location and regional geology of SW Barents Sea. The map is modified after information found in the Norwegian Petroleum Directorate fact page http://www.npd.no/en/. (B) A time-structure map of the base syn-kinematic unit (H4) with a white-dashed line indicating the location of the seismic section in Fig. 2. The location of wellbore 7124/4-1S is noted by a green star while the study area is outlined by the blue border.

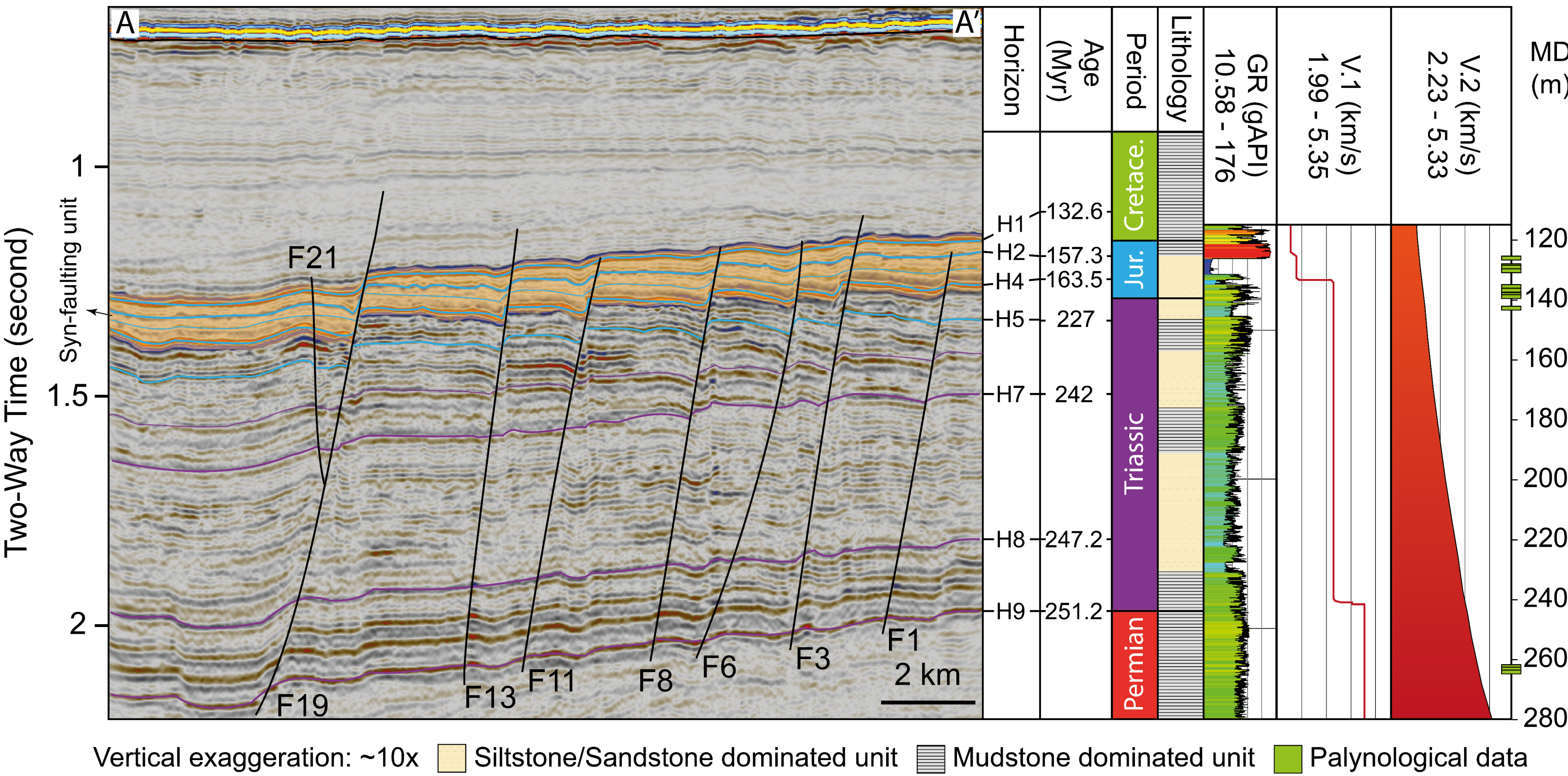

Figure 2: A representative seismic cross-section highlighting the geometry of the studied faults and horizon's age and lithology as constrained by wellbore 7124/4-1S. The section also includes Gamma Ray (GR) log data, modelled interval velocity using simplified geological model (V.1) and calculated pseudo interval velocity using estimated time-depth relationship from seismic well tie (V.2).

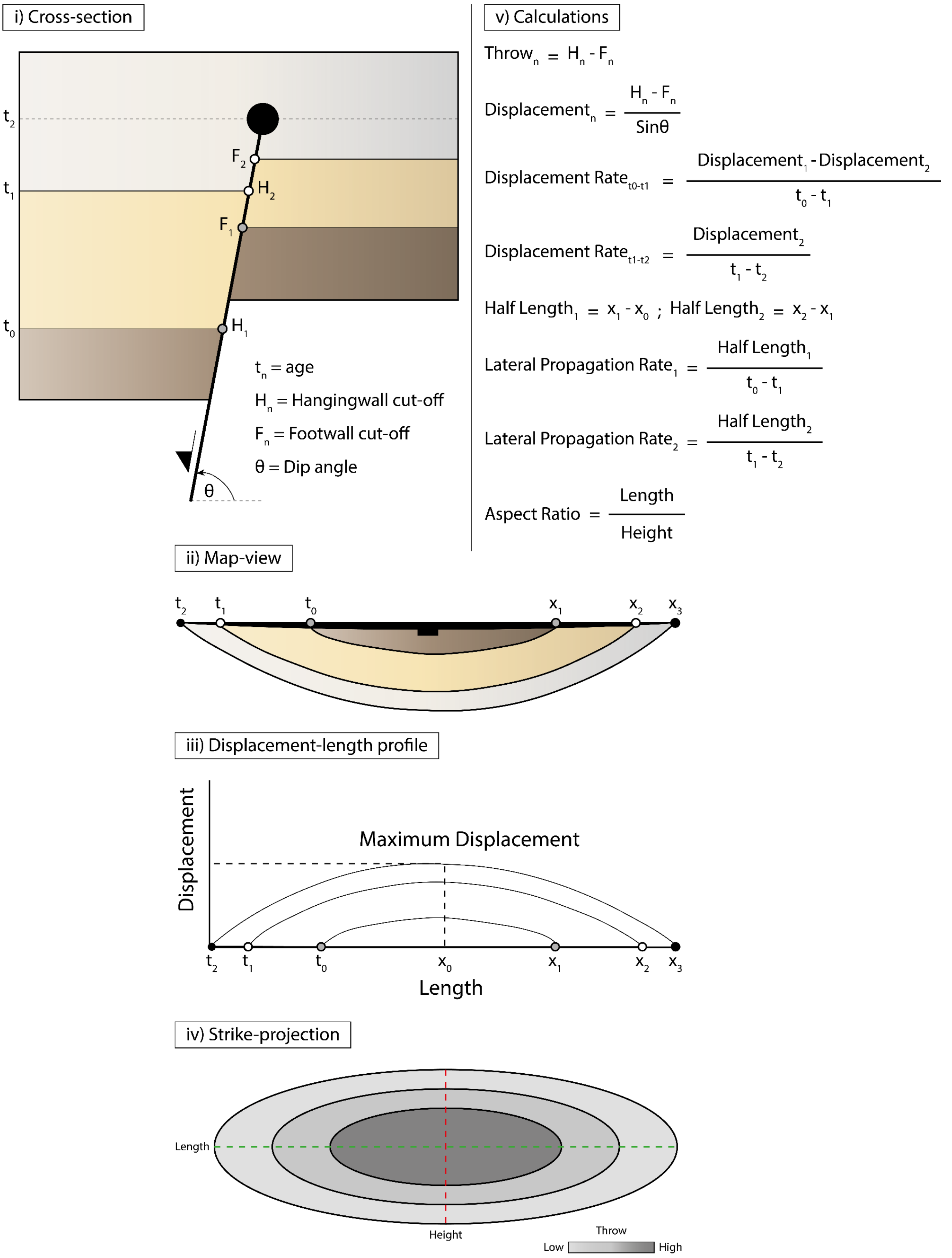

Figure 3: Detailed description of the methodology we use to calculate fault throw, displacement, displacement accumulation rate (Displacement Rate), lateral propagation rate (Lateral Propagation Rate), and fault length / height aspect ratio (Aspect Ratio).

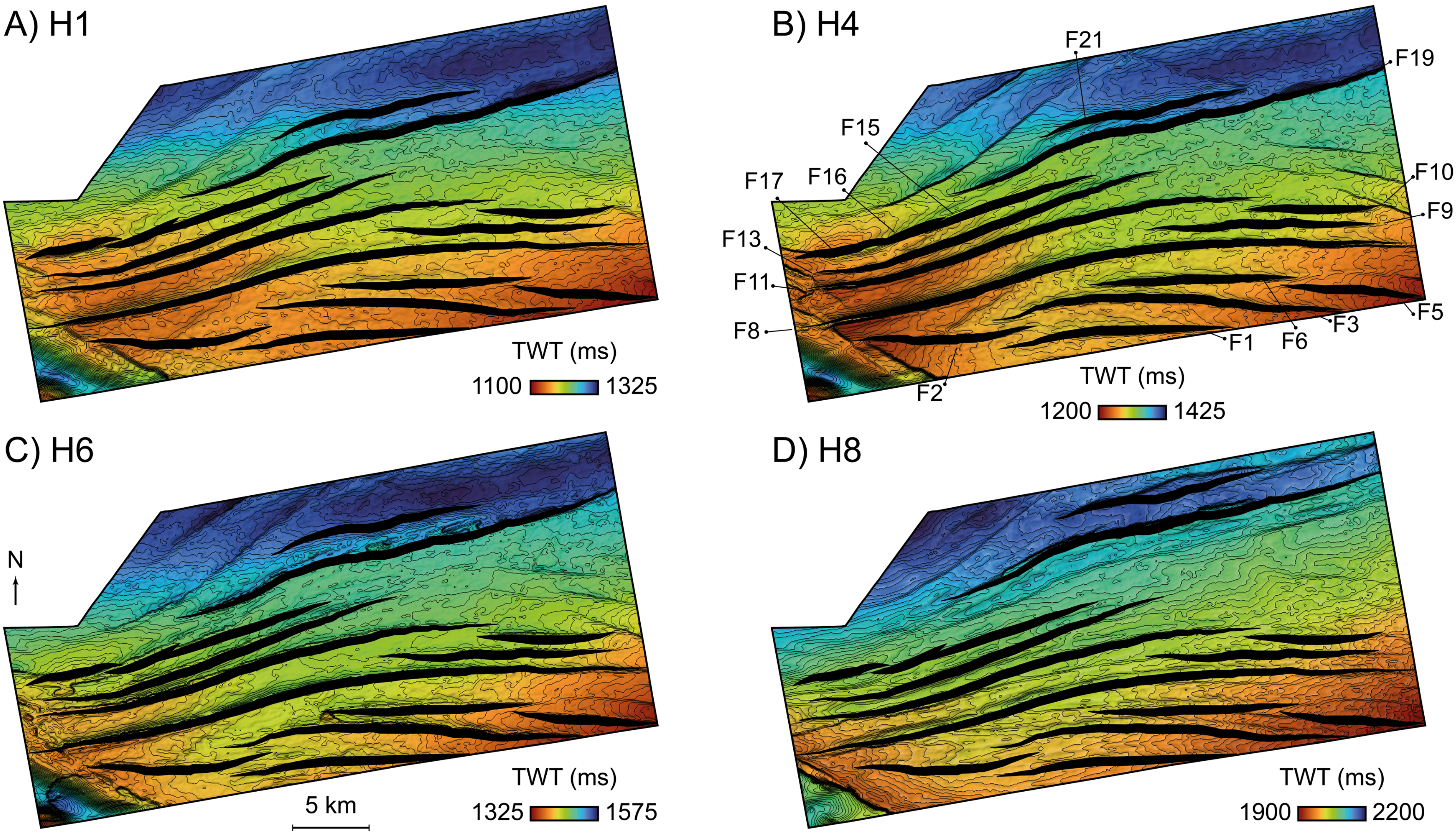

Figure 4: Time-structure maps for the Early Cretaceous (H1), Middle Jurassic (H4), Middle Triassic (H6) and Lower Triassic (H8) horizons. The location of the fault network and names of the studied faults are annotated on (B).

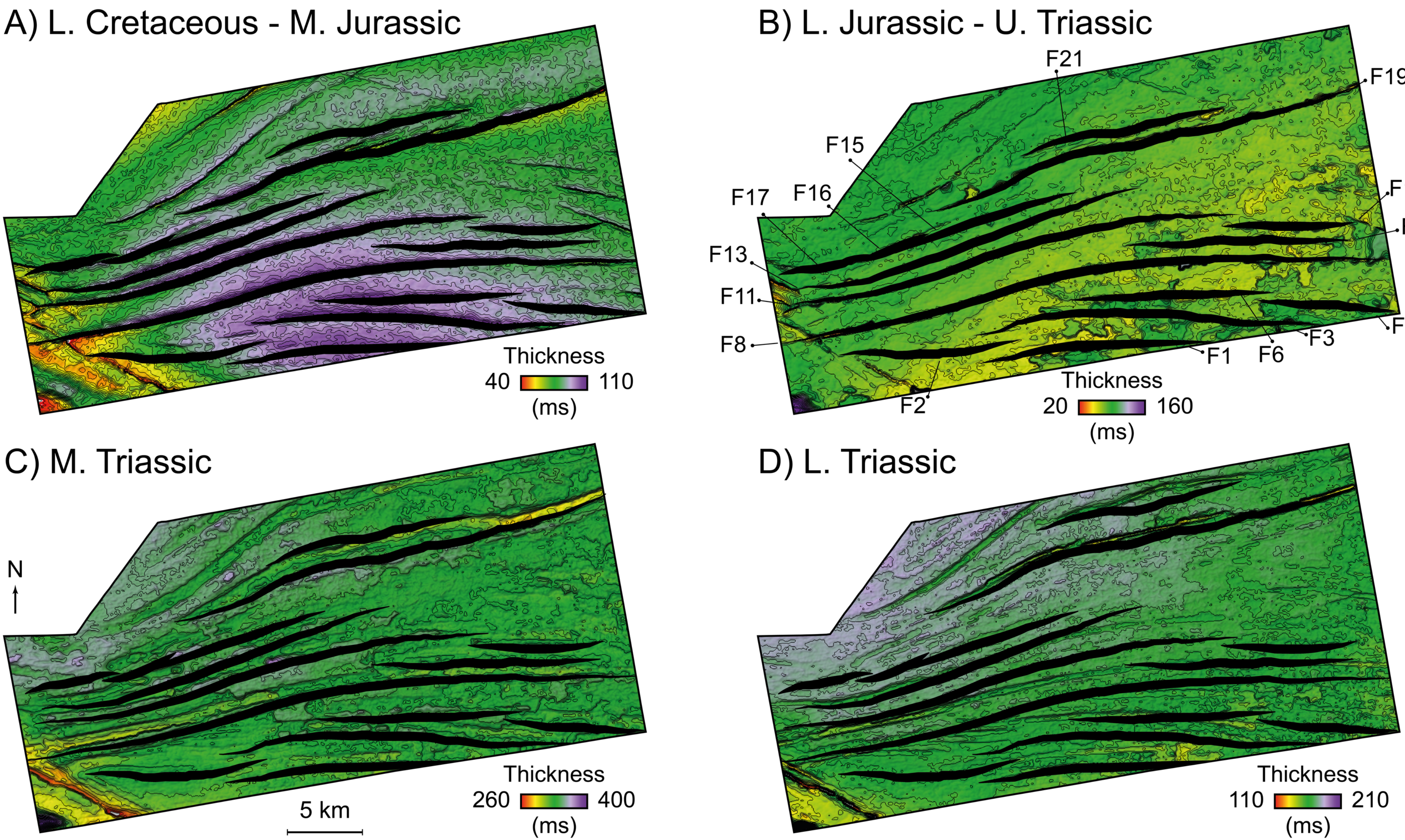

Figure 5: Isochron (time-thickness) maps for the L. Cretaceous to M. Jurassic **(A)**, L. Jurassic to U. Triassic **(B)**, M. Triassic **(C)** and L. Triassic **(D)**. These isochrons show the clear across-fault thickening in the Early Cretaceous to Middle Jurassic and general constant thickness nature of the other time intervals.

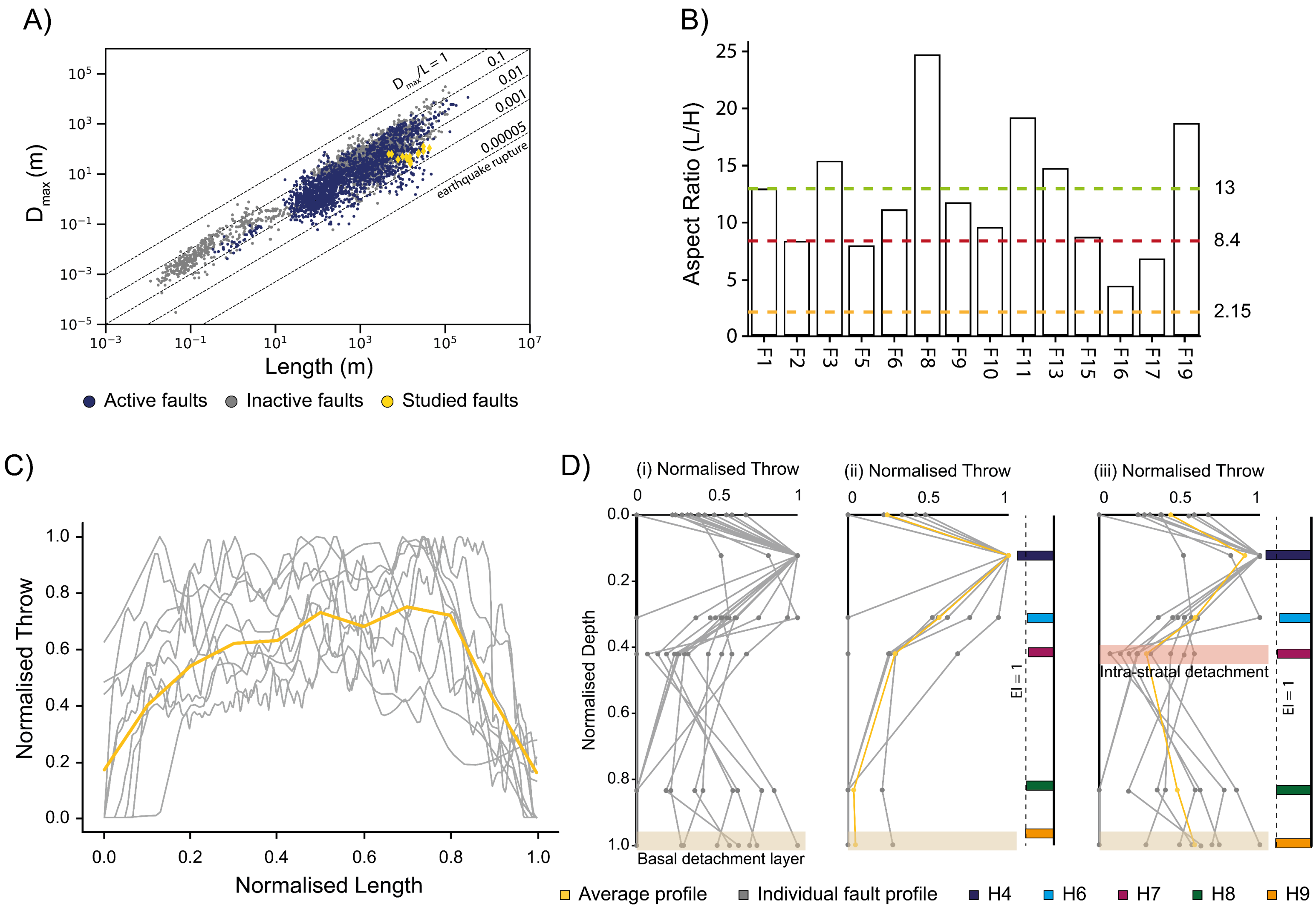

Figure 6: A summary of the geometric properties of the fault network showing **(A)** D_{max}-L_{max} plot from a global database of normal faults (modified after Lathrop et al., 2022). Data for studied fault network are shown in yellow while literature data are showing in blue (active faults) and grey (inactive faults). **(B)** Aspect ratio (length/height) distribution of the studied fault network with dashed-horizontal lines showing average aspect ratios of "blind isolated normal faults in layered sequences" (yellow), maximum aspect ratio of restricted faults (red) (Nicol et al., 1996) and maximum aspect ratio for faults cutting formations with strong mechanical contrast (green) (Roche et al., 2013). **(C)** Normalized throw-length plot for the studied faults (grey) at the base syn-kinematic level (H4) with an average profile of the fault network shown in yellow. **(D)** Normalized throw-depth profiles for the studied faults showing the basal detachment layer **(i)**. The fault network can be divided into two subsets with subset 1 including faults F1, F5, F8, F10, F17 and F21 **(ii)** showing a single throw maximum at the H4 level while subset 2 (F2, F3, F6, F9, F11, F13, F15, F16, and F19) **(iii)** shows the presence of a potential intra-stratal detachment layer that separates two throw maxima denoting potential vertical (i.e., dip) linkage. The Expansion Index (EI) values of H4, H6, H7, H8 and H9 are shown to the side of the normalized throw-depth plots.

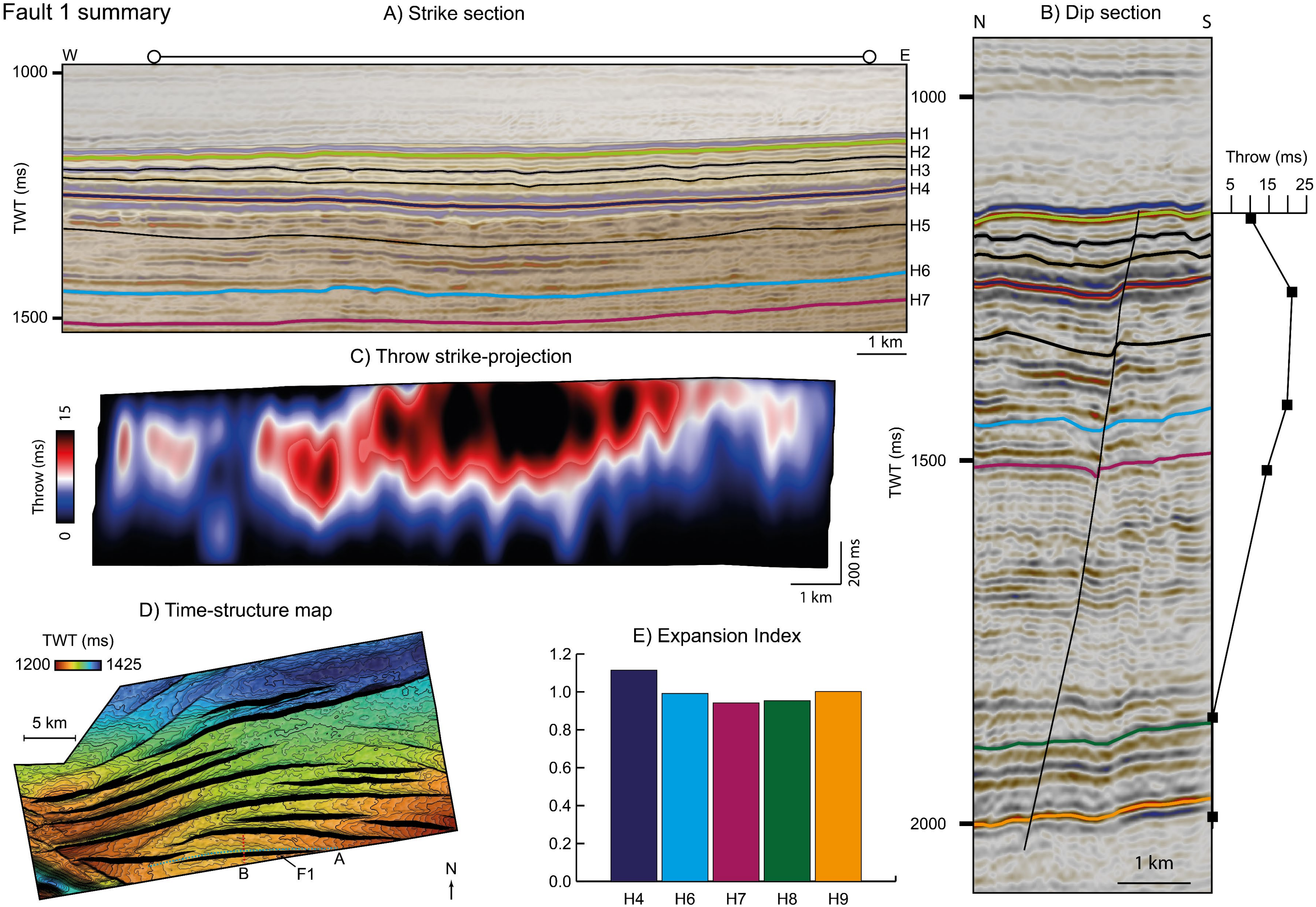

Figure 7: A detailed overview of Fault 1 (F1) showing **(A)** a strike-parallel seismic section, **(B)** a strike-perpendicular (dip) seismic section, **(C)** strike-projected throw distribution along the fault surface, **(D)** A time-structure map of the base syn-kinematic horizons (H4) denoting the fault map location and the location of sections **(A)** and **(B)**. **(E)** Expansion Index (EI) values showing potential across fault thickening (i.e., syn-kinematic growth) at the H4 level.

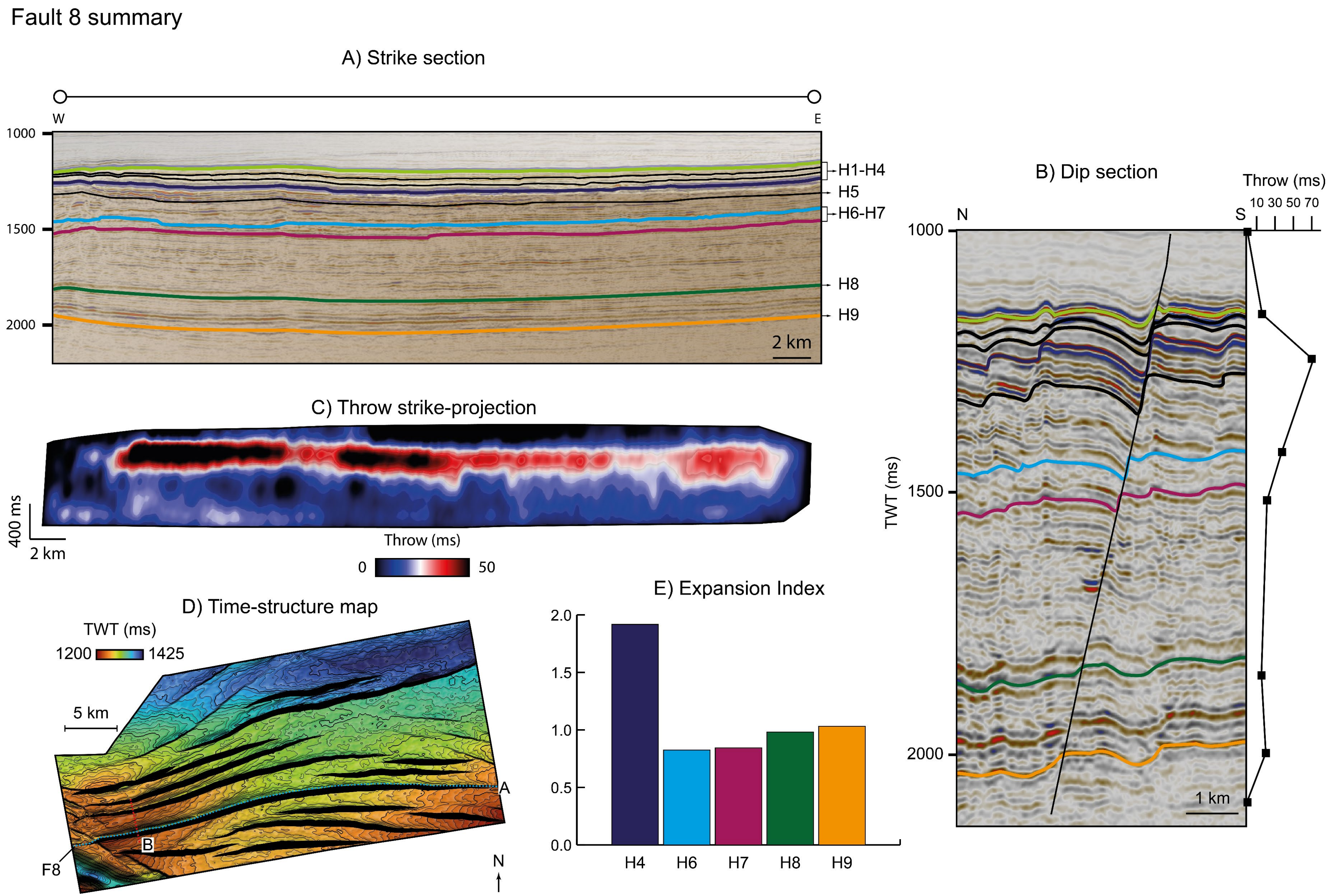

Figure 8: A detailed overview of Fault 8 (F8) showing **(A)** a strike-parallel seismic section, **(B)** a strike-perpendicular (dip) seismic section, **(C)** strike-projected throw distribution along the fault surface, **(D)** A time-structure map of the base syn-kinematic horizons (H4) denoting the fault map location and the location of sections **(A)** and **(B)**. **(E)** Expansion Index (EI) values showing potential across fault thickening (i.e., syn-kinematic growth) at the H4 level.

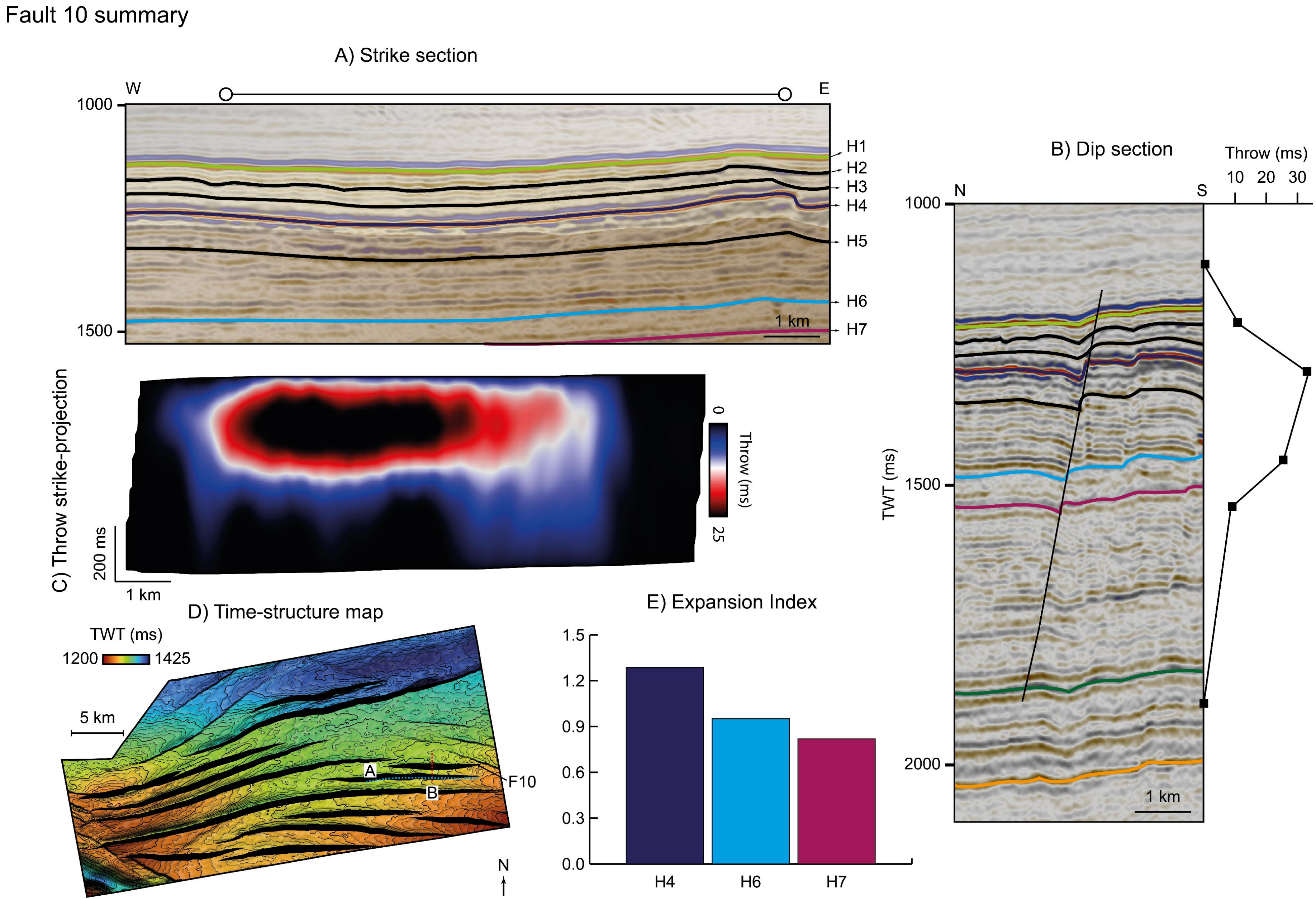

Figure 9: A detailed overview of Fault 10 (F10) showing **(A)** a strike-parallel seismic section, **(B)** a strike-perpendicular (dip) seismic section, **(C)** strike-projected throw distribution along the fault surface, **(D)** A time-structure map of the base syn-kinematic horizons (H4) denoting the fault map location and the location of sections **(A)** and **(B)**. **(E)** Expansion Index (EI) values showing potential across fault thickening (i.e., syn-kinematic growth) at the H4 level.

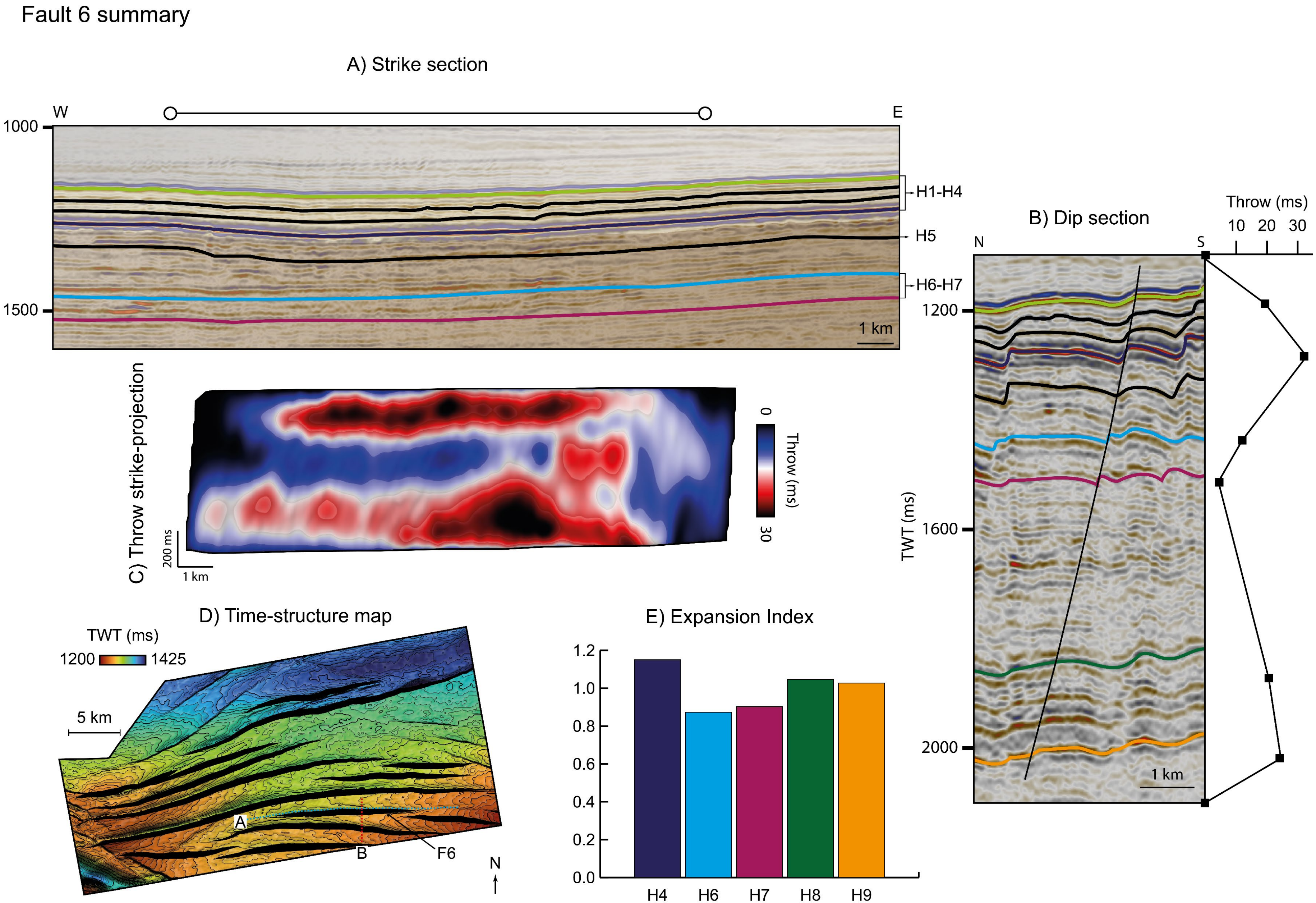

Figure 10: A detailed overview of Fault 6 (F6) showing **(A)** a strike-parallel seismic section, **(B)** a strike-perpendicular (dip) seismic section, **(C)** strike-projected throw distribution along the fault surface, **(D)** A time-structure map of the base syn-kinematic horizons (H4) denoting the fault map location and the location of sections **(A)** and **(B)**. **(E)** Expansion Index (EI) values showing potential across fault thickening (i.e., syn-kinematic growth) at the H4 level.

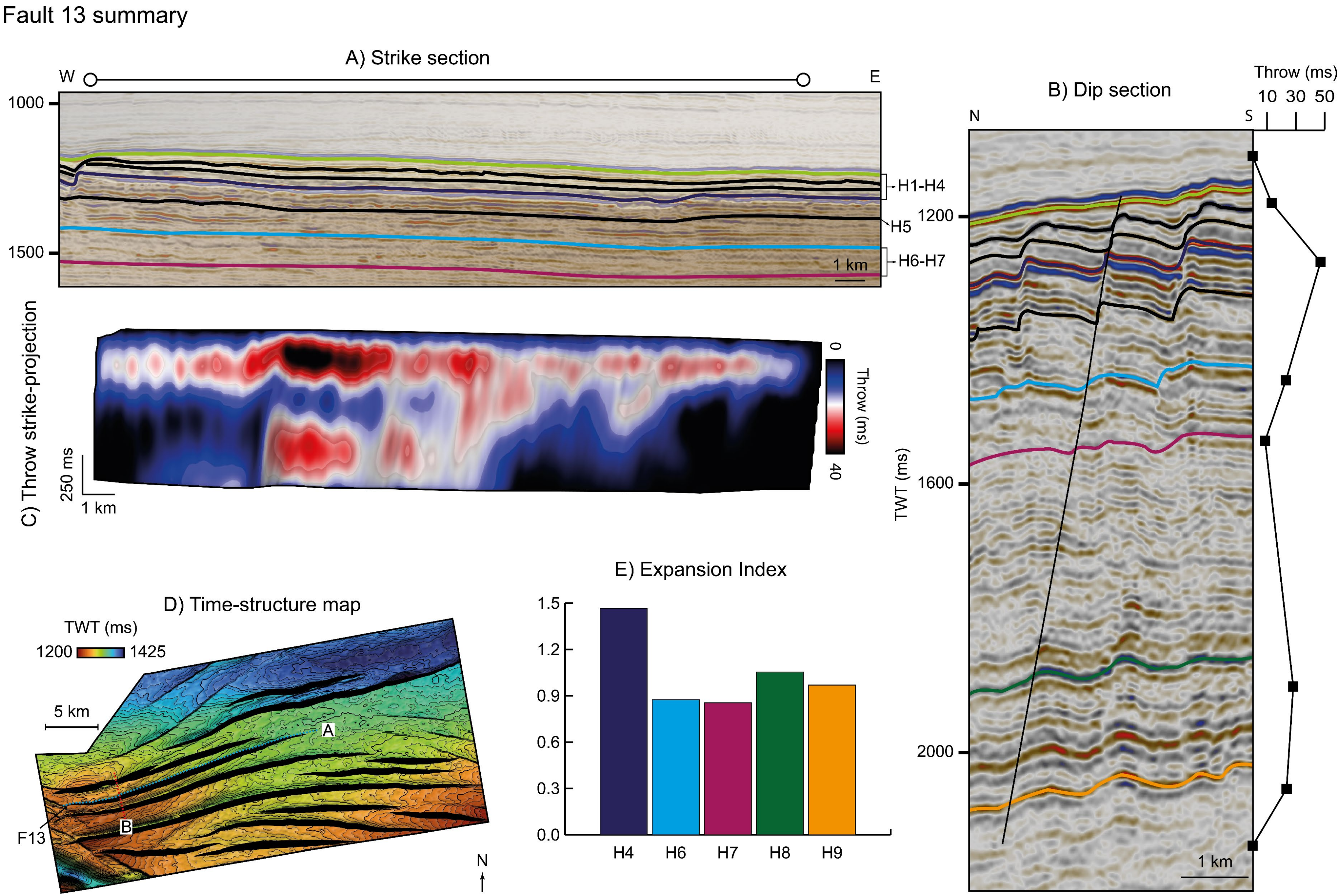

Figure 11: A detailed overview of Fault 11 (F11) showing **(A)** a strike-parallel seismic section, **(B)** a strike-perpendicular (dip) seismic section, **(C)** strike-projected throw distribution along the fault surface, **(D)** A time-structure map of the base syn-kinematic horizons (H4) denoting the fault map location and the location of sections **(A)** and **(B)**. **(E)** Expansion Index (EI) values showing potential across fault thickening (i.e., syn-kinematic growth) at the H4 level.

Fault 19 summary

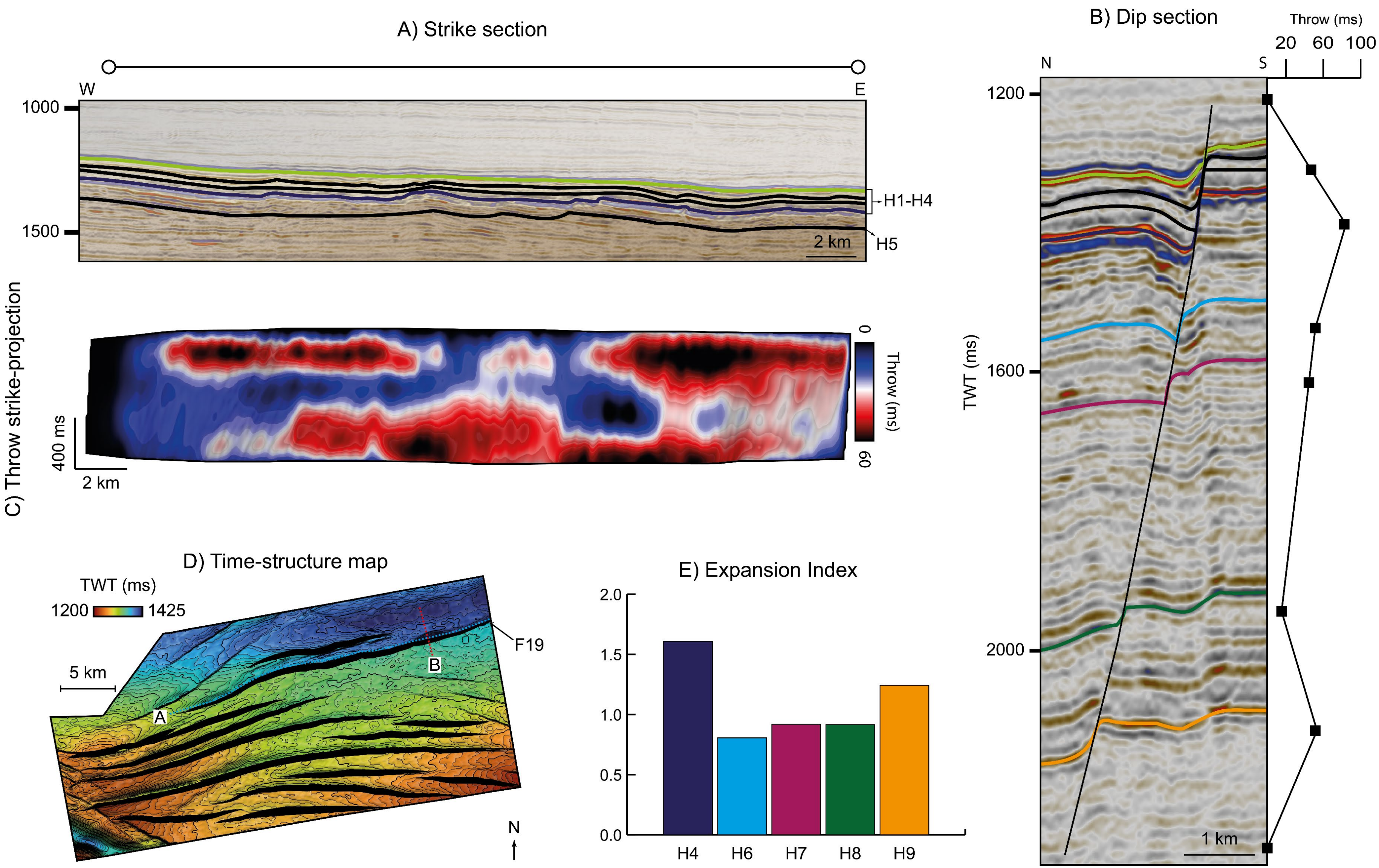

Figure 12: A detailed overview of Fault 19 (F19) showing **(A)** a strike-parallel seismic section, **(B)** a strike-perpendicular (dip) seismic section, **(C)** strike-projected throw distribution along the fault surface, **(D)** A time-structure map of the base syn-kinematic horizons (H4) denoting the fault map location and the location of sections **(A)** and **(B)**. **(E)** Expansion Index (EI) values showing potential across fault thickening (i.e., syn-kinematic growth) at the H4 level.

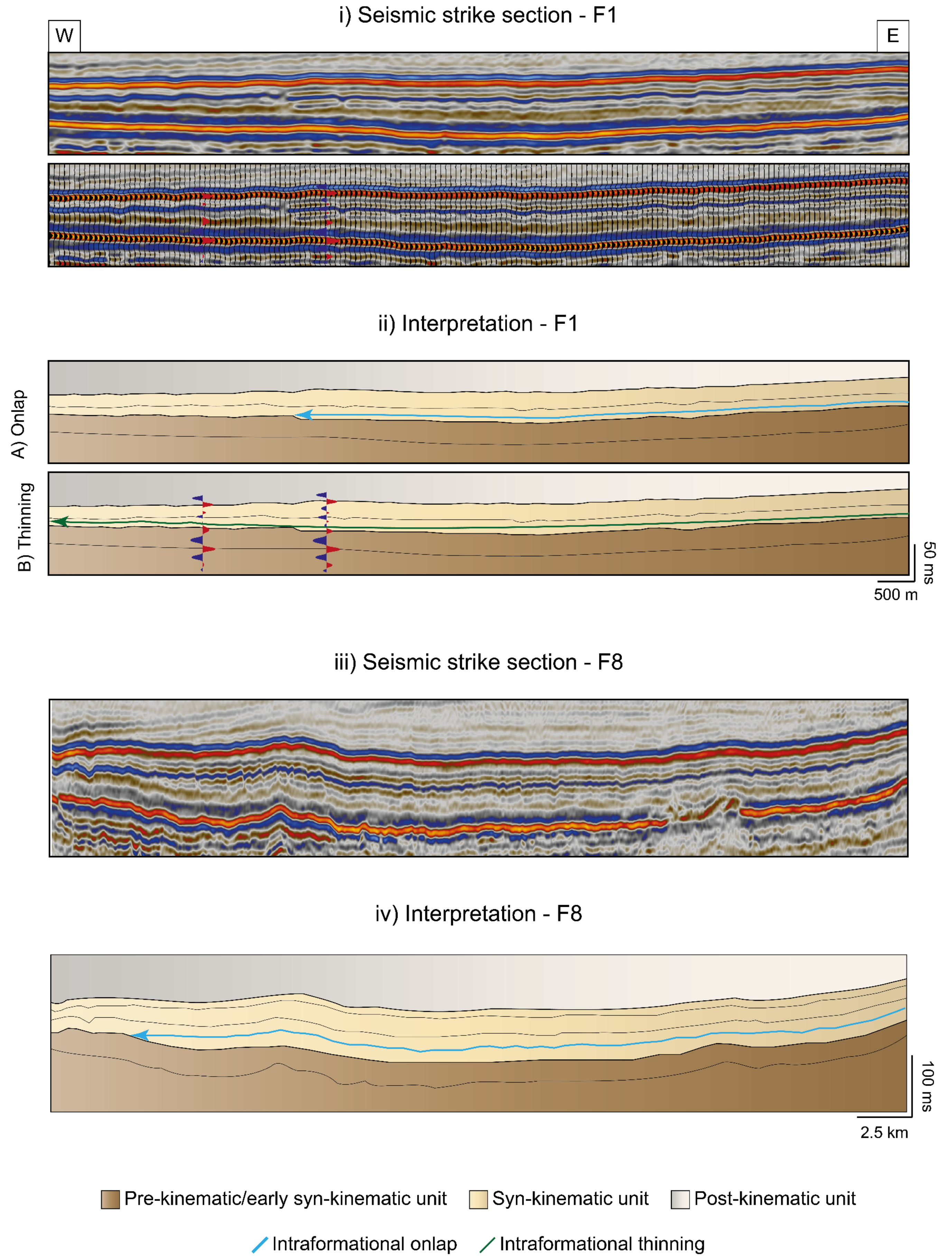

Figure 13: Un-interpreted and interpreted strike-parallel sections along faults F1 **(i, ii)** and F8 **(iii, iv)** showing the lowermost reflections in Upper Jurassic package onlapping onto the base syn-kinematic horizon immediately adjacent to the fault tips (blue arrow). **(ii.A, ii.B)** A schematic representation of two possible interpretations along strike of F1 where the blue arrow shows the onlap and truncation scenario before the fault tip and the green arrow shows the onlap and thinning case towards the fault tip. The two interpretations **(ii.A, ii.B)** illustrate the implication of seismic tuning on the observations of the intraformational architecture.

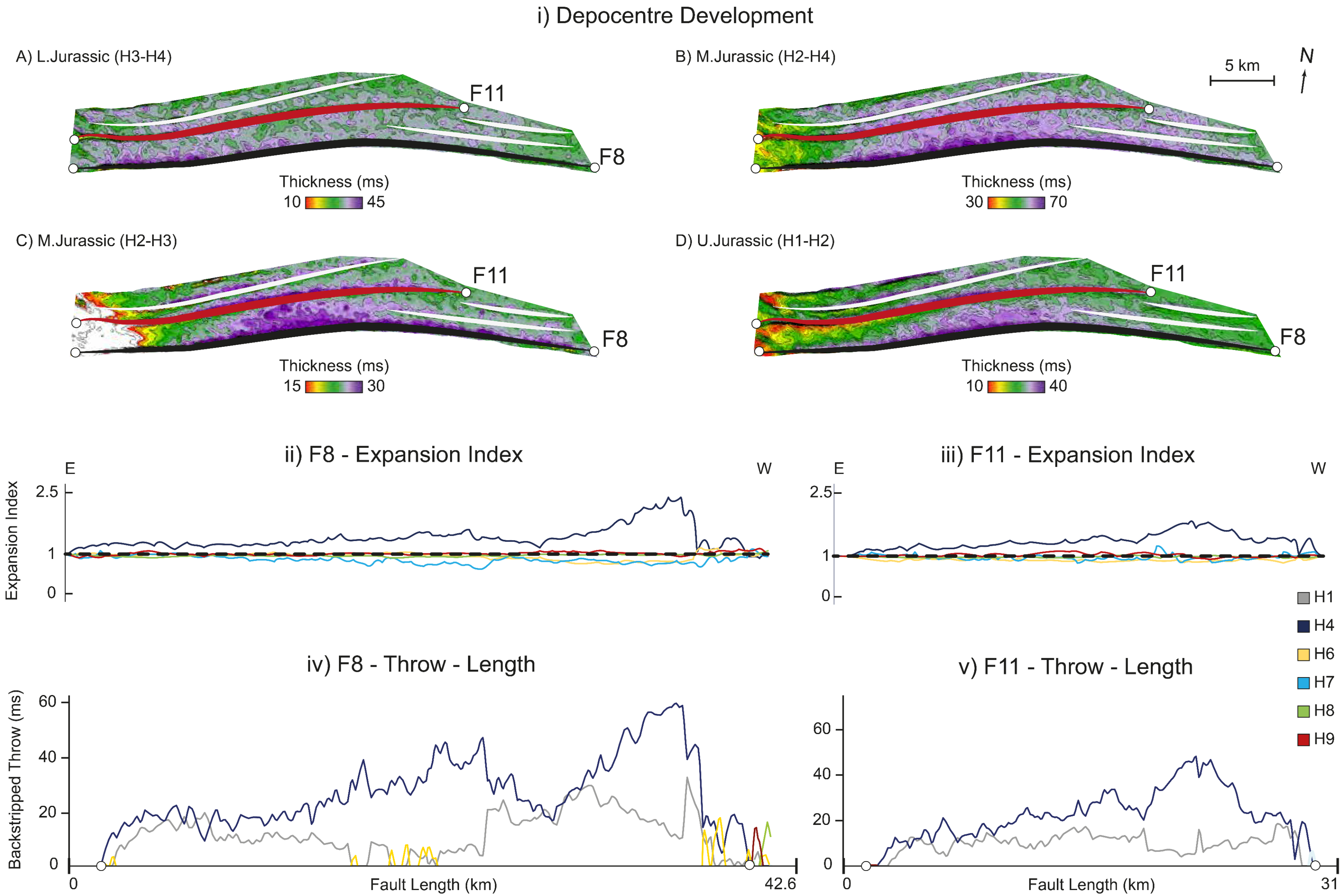

Figure 14: (i) Isochron (time-thickness) maps for sub-units of the syn-kinematic interval (Middle Jurassic to Early Cretaceous) showing across-fault thickening in the smallest resolvable interval. **(ii)** and **(iii)** Expansion Index (EI) values along strike of faults 8 (F8) and 11 (F11) showing values >1 along at the H4 level along strike of the entire fault surface. **(iv)** and **(v)** backstripped throw vs. length profiles for F8 and F11 highlighting maximum throw occurring at H4 level and showing the location of the fault tips.

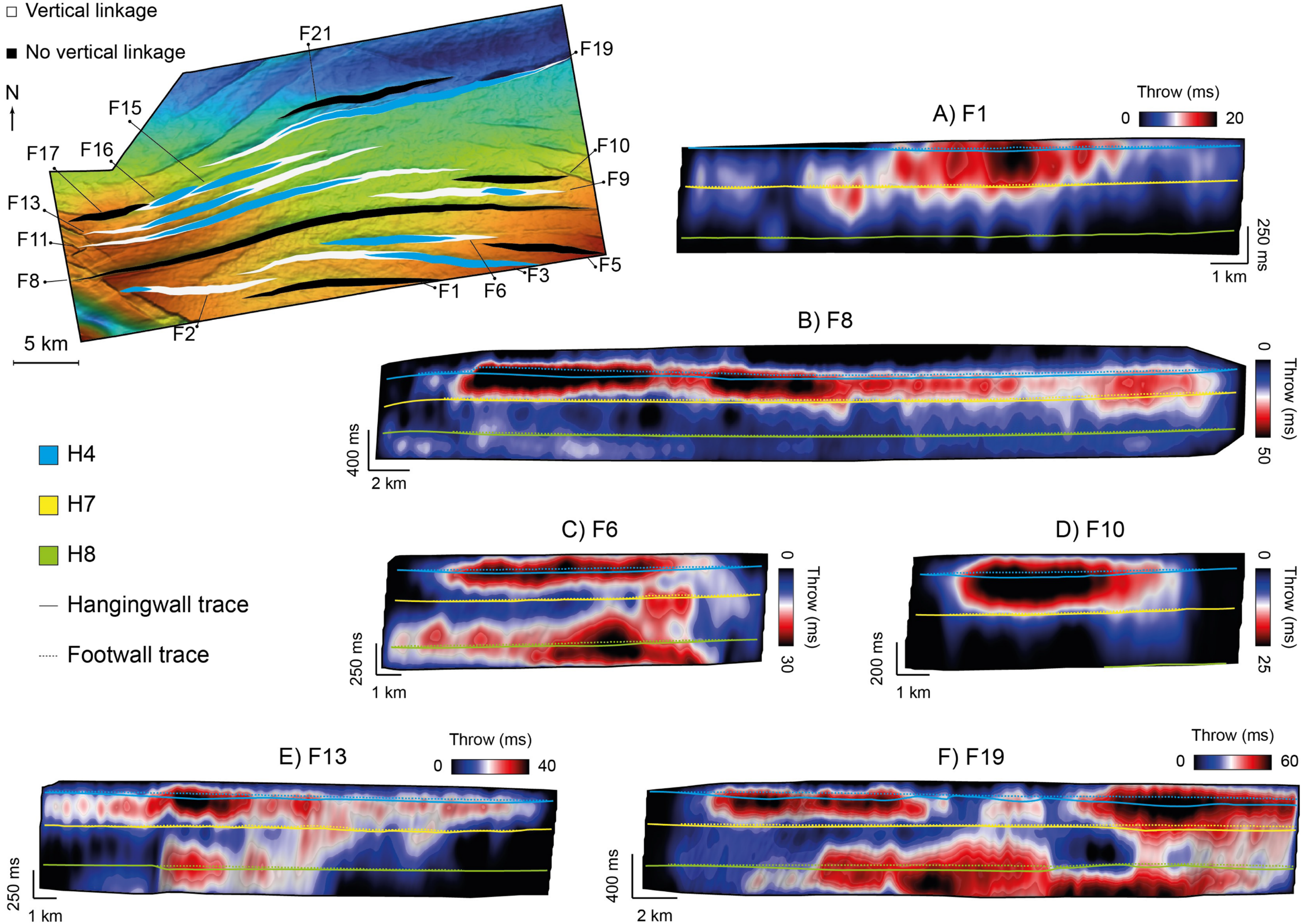

Figure 15: Time-structure map of the base syn-kinematic level (H4) showing the studied fault network. Faults coloured in black are the ones that show no sign of vertical linkage while faults coloured in white indicate faults that exhibit vertical linkage. The blue fill-colour within the white faults highlights the map location of the inferred vertical linkage. Strike-projections A-F show the fault examples discussed in-text with hangingwall and footwall throw traces indicated by solid and dashed lines for horizons H4, H7, and H8. The strike-projections illustrate the lack of any throw maxima below H7 for subset 1 faults (F1, F8, F10) and the presence of an intraformational detachment layer at H7 that separates different throw maxima above and below the detachment for subset 2 faults (F6, F11, F13).

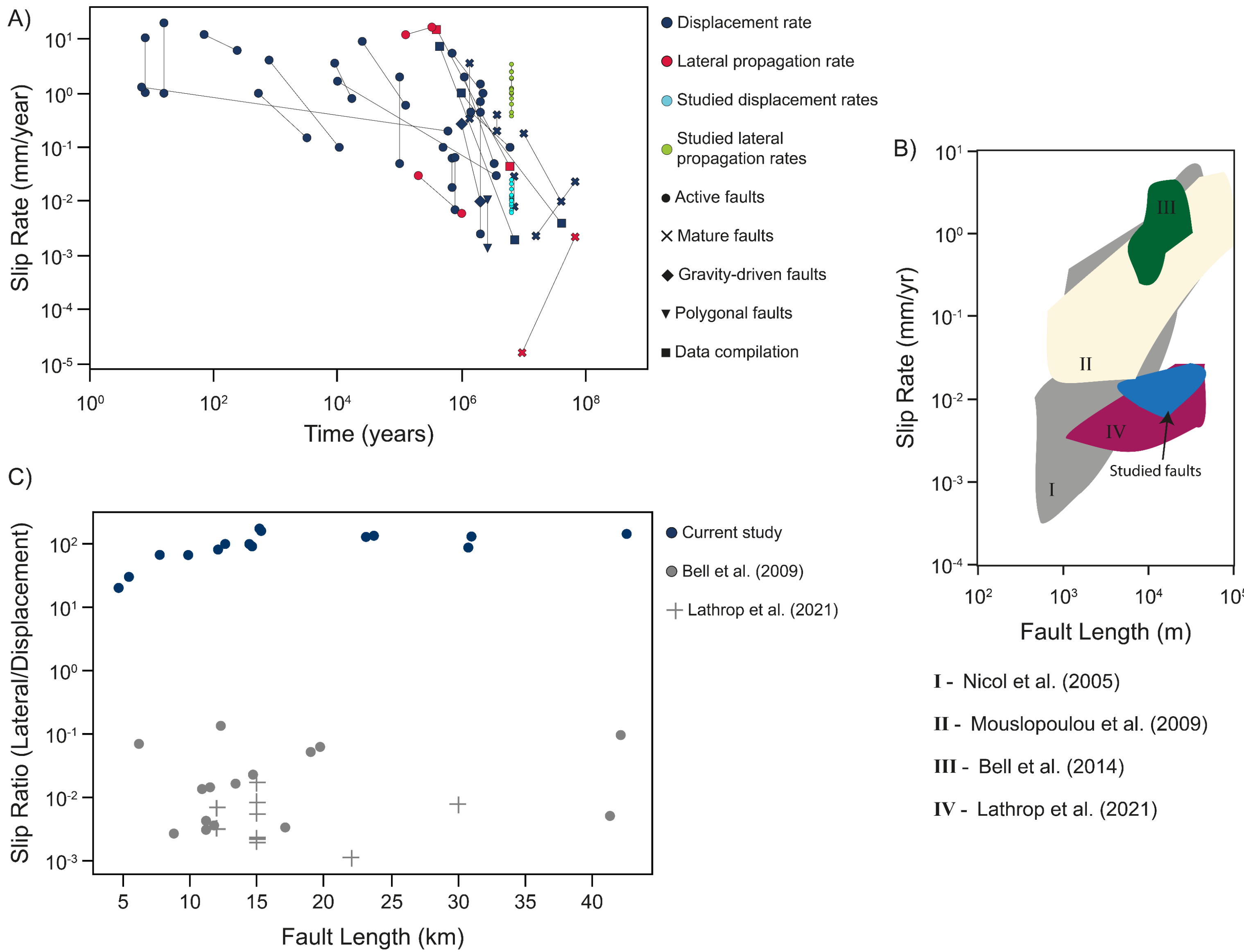

Figure 16: (A) Slip rate data across various timescales for the studied fault network (displacement rates in light blue and lateral propagation rates in light green) and literature data (displacement rates in dark blue and lateral propagation rates in red). The shape of the literature data points relates to their type/origin. Each literature study is represented by two points marking the maximum and minimum reported rates in the study and the line connecting the two points captures the range of reported data by each study. Another version of this plot is provided in Appendix 4 where each literature study is clearly indicated, and the literature data is provided in Appendix 5. **(B)** Slip rate data (displacement rates) across various fault lengths. **(C)** A plot of the ratio of lateral propagation and displacement rates for the studied faults (dark blue), data from Bell et al. (2009) (grey circles) and Lathrop et al. (2021) (grey crosses). The plot shows that the studied fault network has a ratio that is 2-3 orders of magnitude higher than other seismically imaged faults of similar length. Please note that we plot the maximum and minimum slip rate data from each study and connect those two points with a line to represent the full range of rates reported (Fig. 16A).

Appendix 1

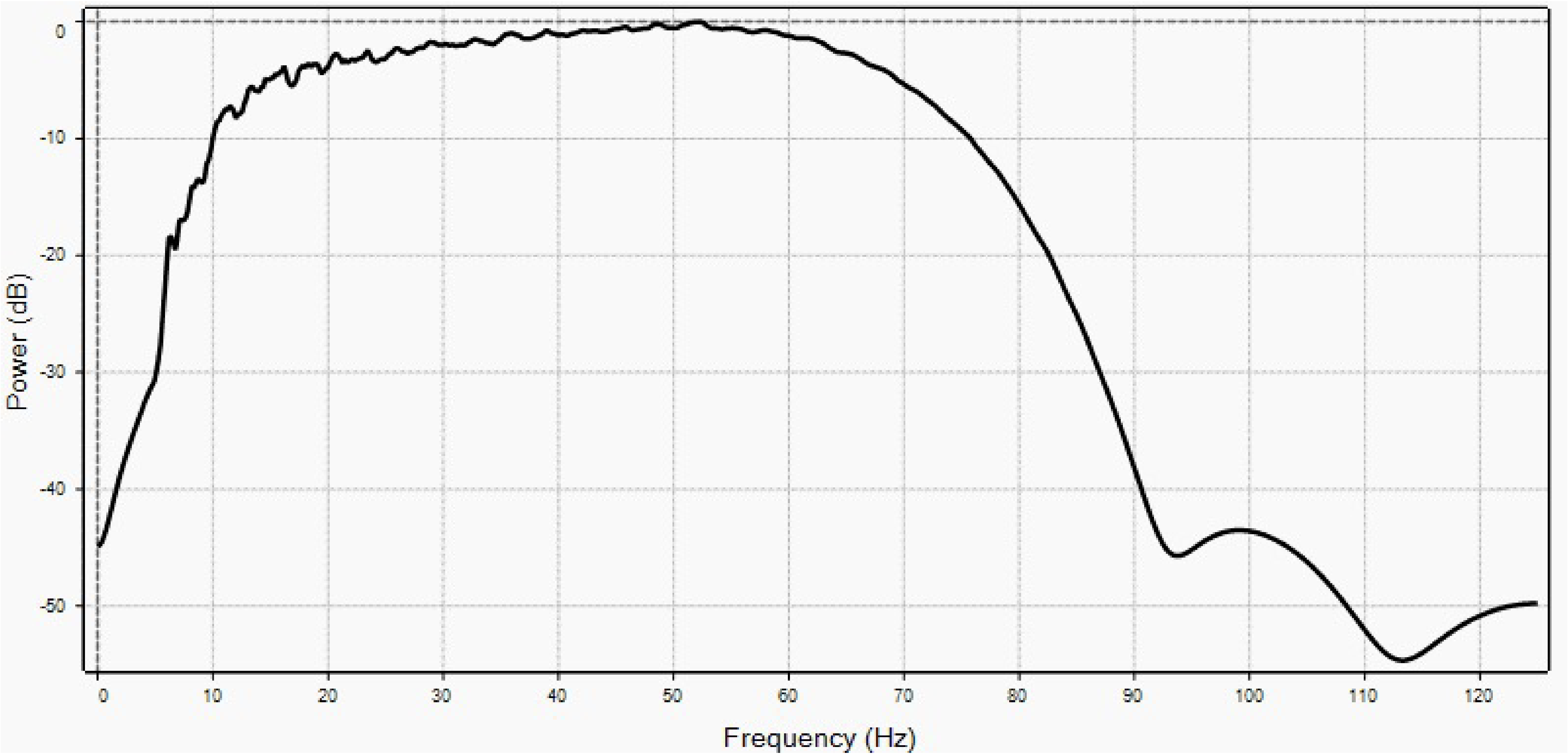

Frequency spectrum for the 3D seismic reflection dataset used in this study. The figure shows that the dominant frequency ranges between 40 – 60 Hz depending on the depth interval within the seismic survey.

Appendix 2 – Palynological samples

Sample number	Sample depth (m)
1	1264
2	1294
3	1297
4	1300
5	1309
6	1360
7	1372
8	1387
9	1399
10	1432
11	2627
12	2657
13	2663

Data source: Norwegian Petroleum Directorate Factpage -
https://factpages.npd.no/en/wellbore/pageview/exploration/all/6678

Appendix 4

A plot showing the compiled data from 29 different studies in addition to data from the current study.
Detailed information about each study are provided in Appendix 5.

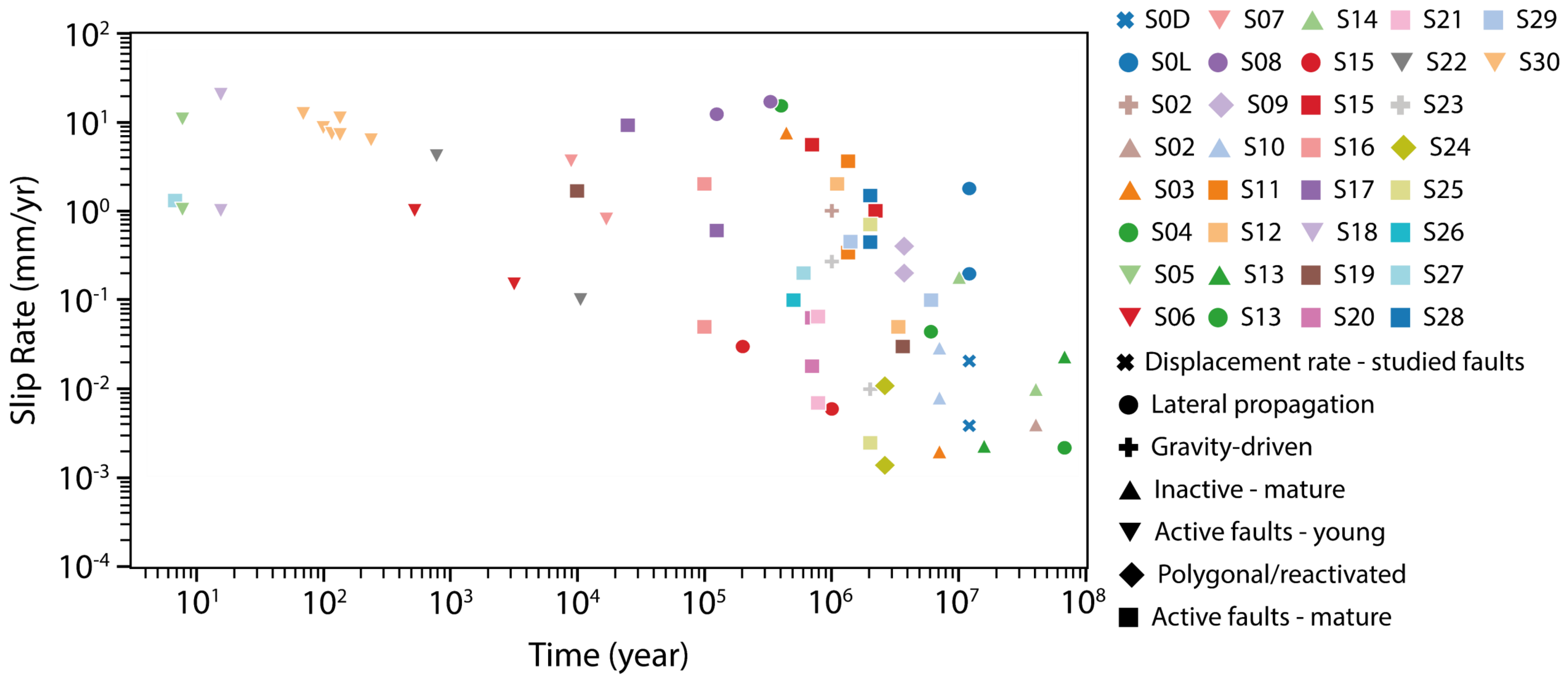

Appendix 7 – A detailed overview of all studied faults 1 **(A)** a strike-parallel seismic section, **(B)** a strike-perpendicular (dip) seismic section, **(C)** strike-projected throw distribution along the fault surface, **(D)** A time-structure map of the base syn-kinematic horizons (H4) denoting the fault map location and the location of sections **(A)** and **(B)**. **(E)** Expansion Index (EI) values showing potential across fault thickening (i.e., syn-kinematic growth) at the H4 level.

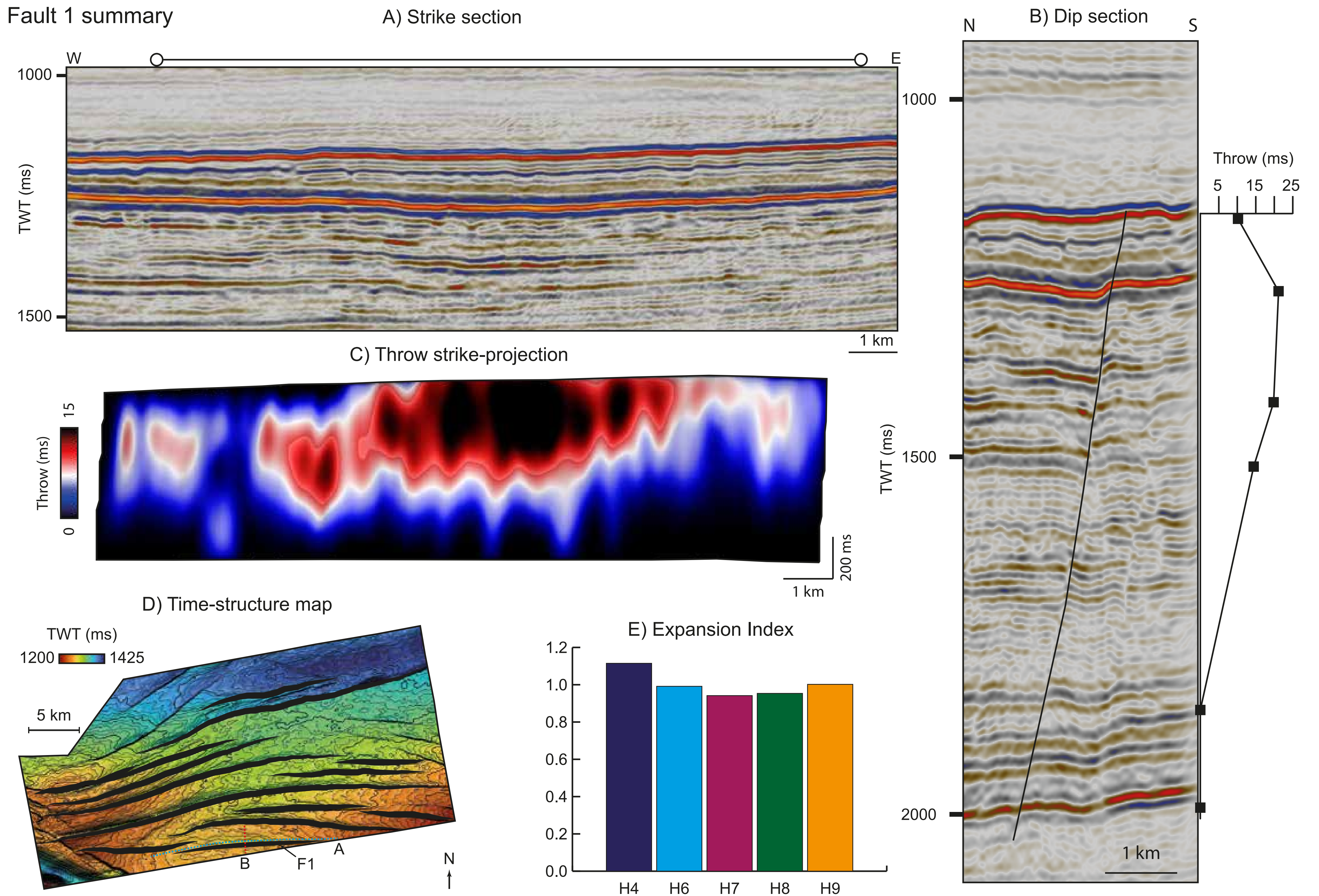

Fault 1 summary
A) Strike section
W
E
1000
1500
TWT (ms)
1 km
B) Dip section
N
S
1000
1500
2000
TWT (ms)
Throw (ms)
5
15
25
1 km
C) Throw strike-projection
Throw (ms)
0
15
200 ms
1 km
D) Time-structure map
TWT (ms)
1200
1425
5 km
B
F1
A
N
E) Expansion Index
1.2
1.0
0.8
0.6
0.4
0.2
0.0
H4
H6
H7
H8
H9

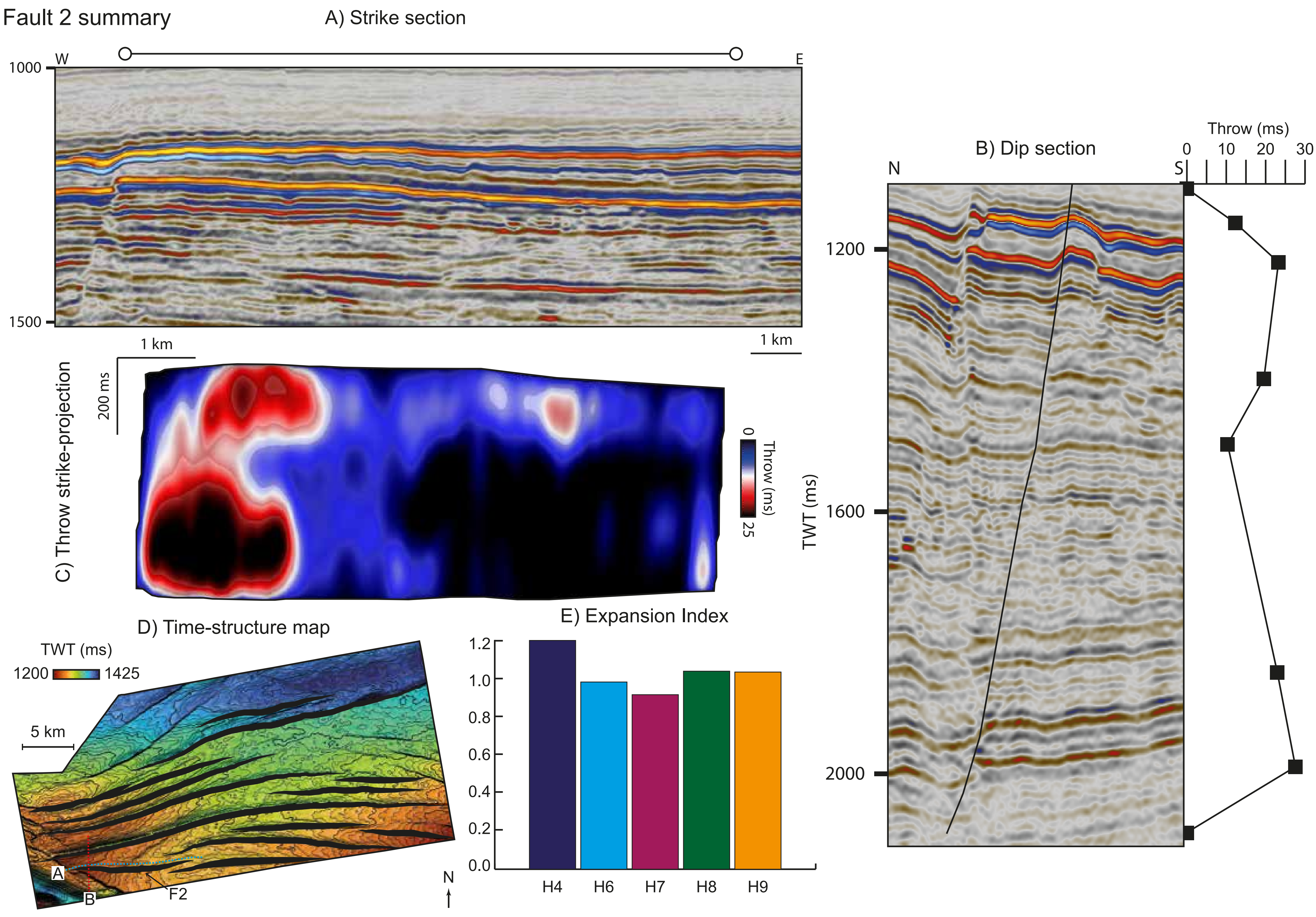

Fault 2 summary
A) Strike section
W
E
1000
1500
1 km
B) Dip section
N
S
Throw (ms)
0
10
20
30
1200
1600
2000
TWT (ms)
C) Throw strike-projection
1 km
200 ms
0
Throw (ms)
25
D) Time-structure map
TWT (ms)
1200
1425
5 km
A
B
F2
N
E) Expansion Index
1.2
1.0
0.8
0.6
0.4
0.2
0.0
H4
H6
H7
H8
H9

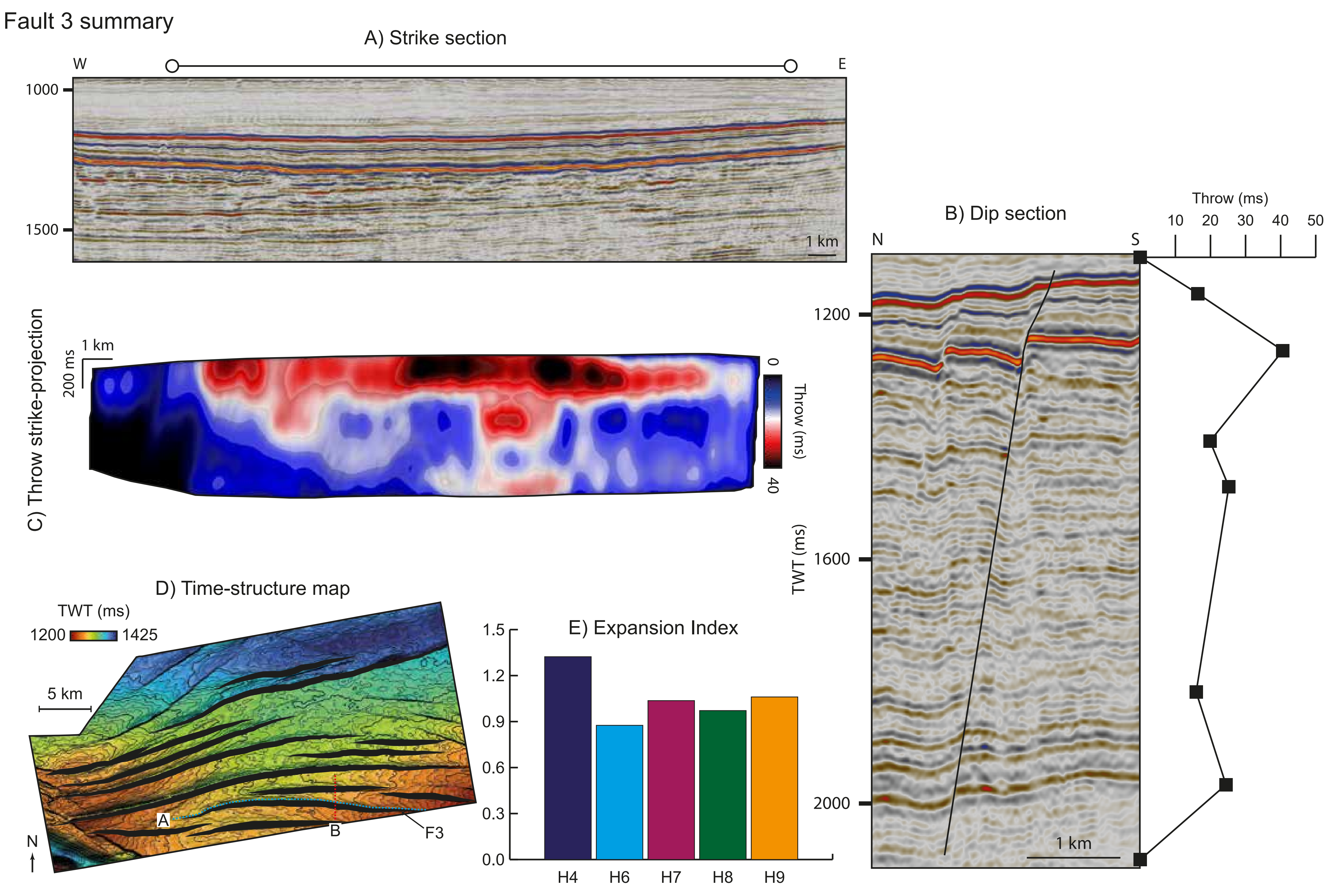

Fault 3 summary
A) Strike section
W
E
1000
1500
1 km
B) Dip section
N
S
Throw (ms)
10
20
30
40
50
1200
1600
2000
TWT (ms)
1 km
C) Throw strike-projection
1 km
200 ms
0
Throw (ms)
40
D) Time-structure map
TWT (ms)
1200
1425
5 km
A
B
F3
N
E) Expansion Index
1.5
1.2
0.9
0.6
0.3
0.0
H4
H6
H7
H8
H9

Fault 5 summary

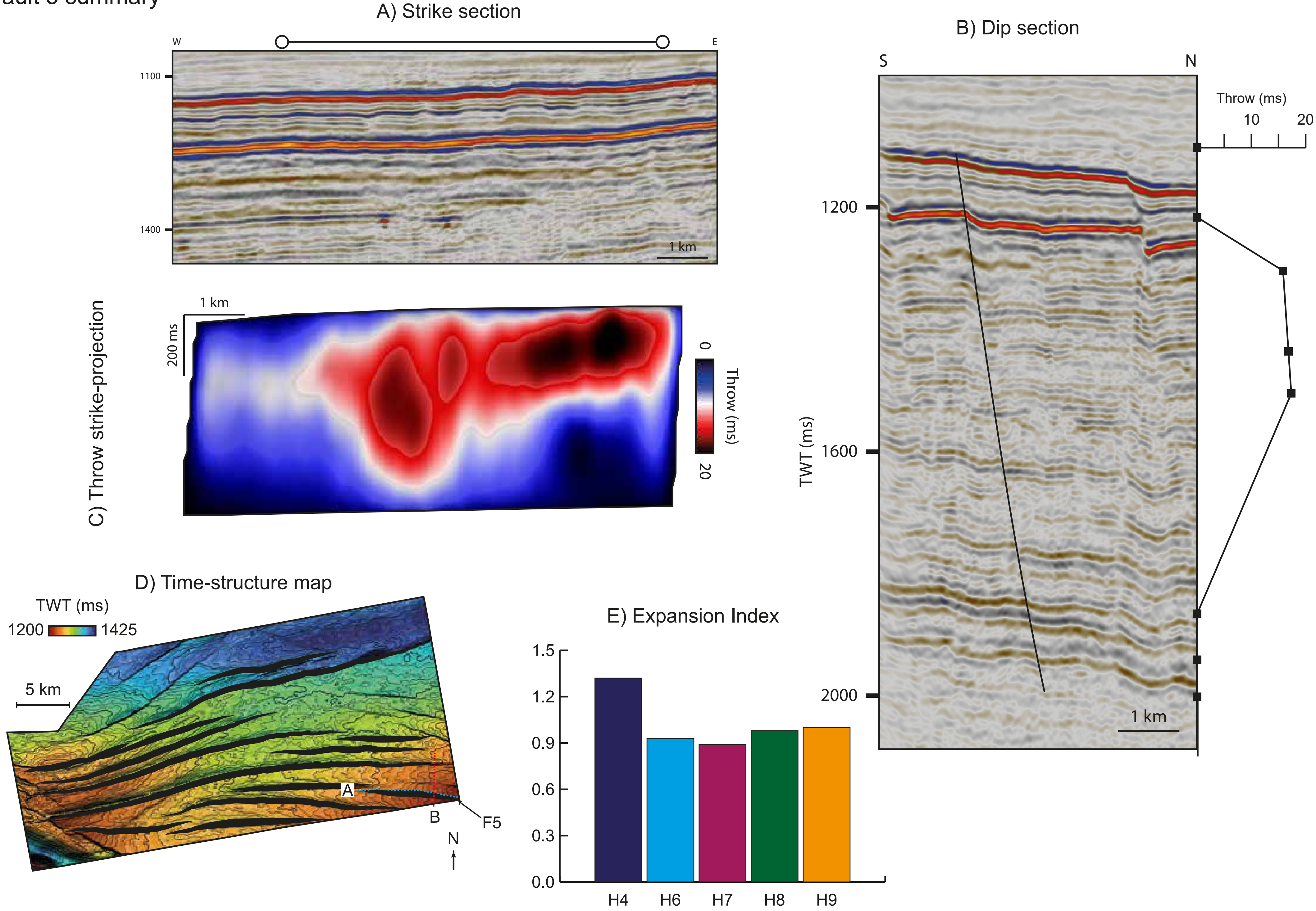

Fault 6 summary

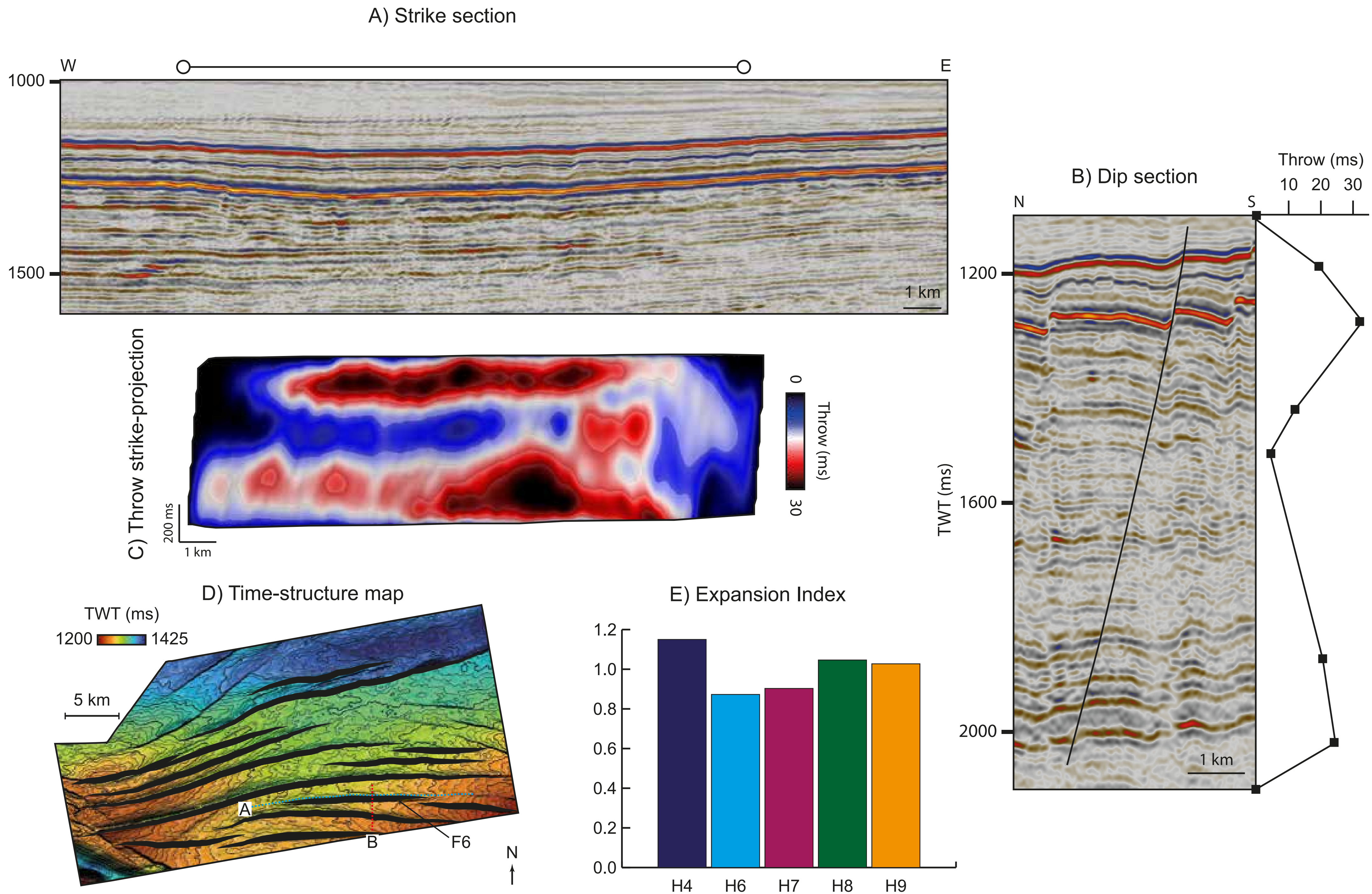

Fault 8 summary

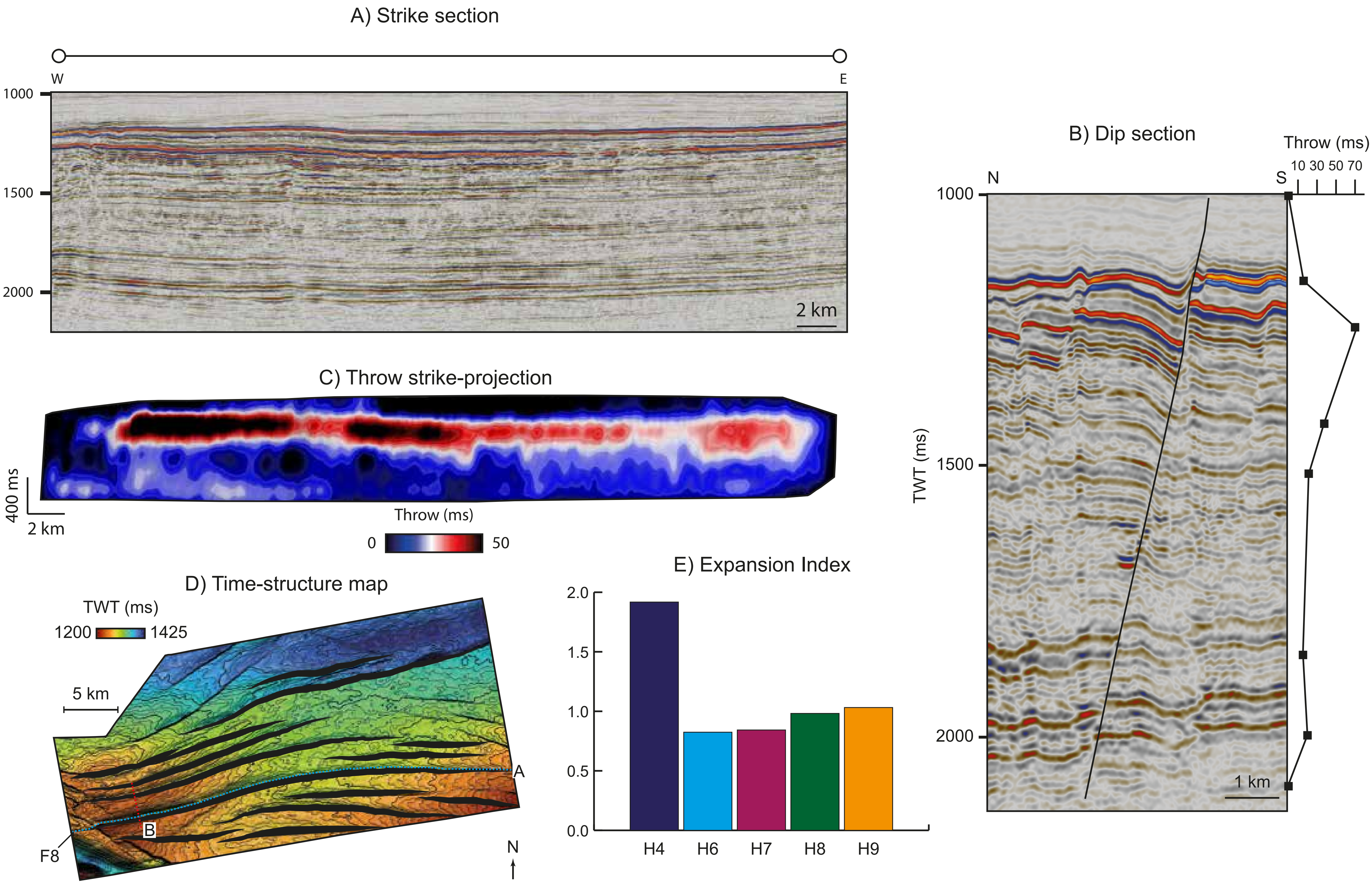

Fault 9 summary

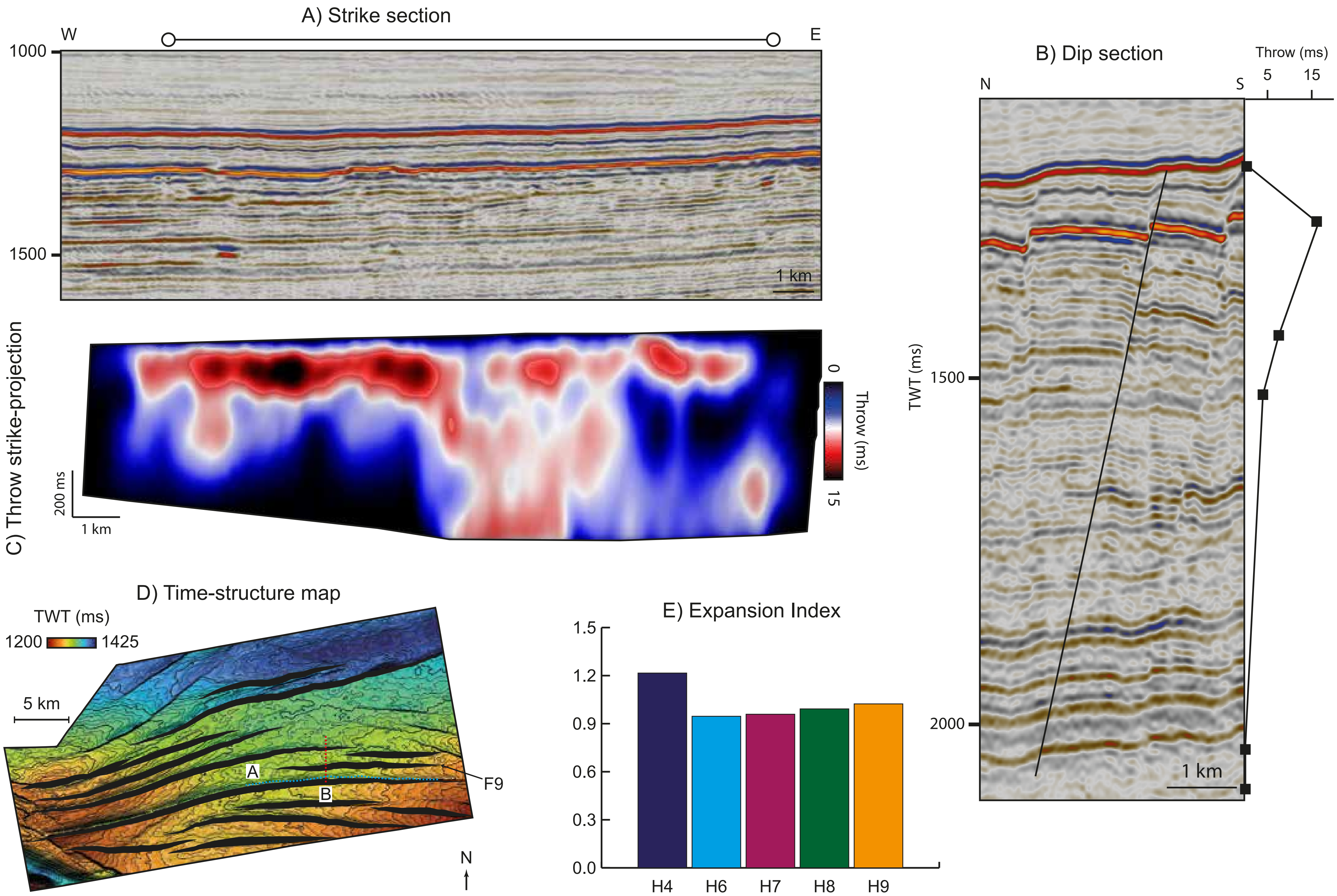

Fault 10 summary

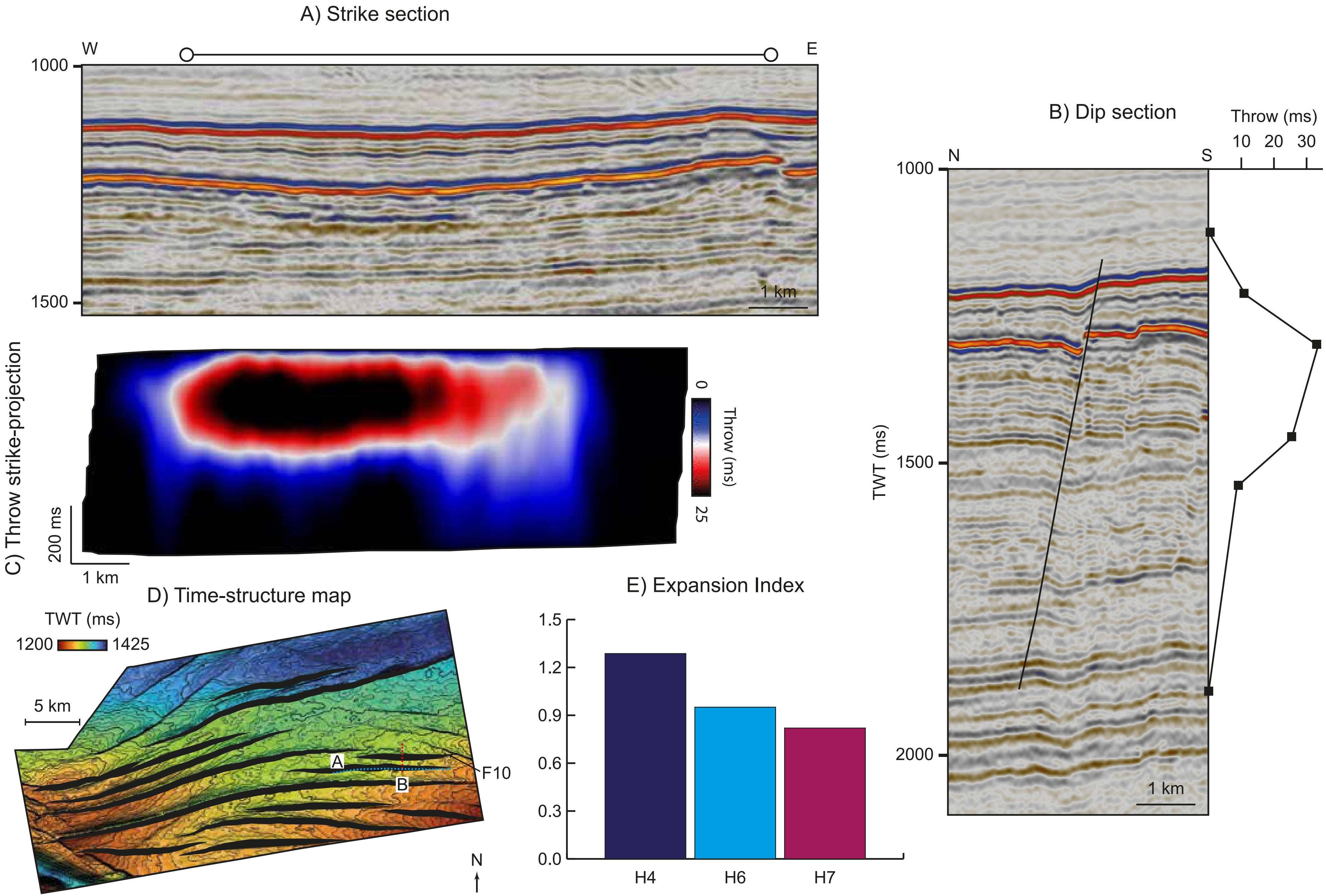

Fault 11 summary

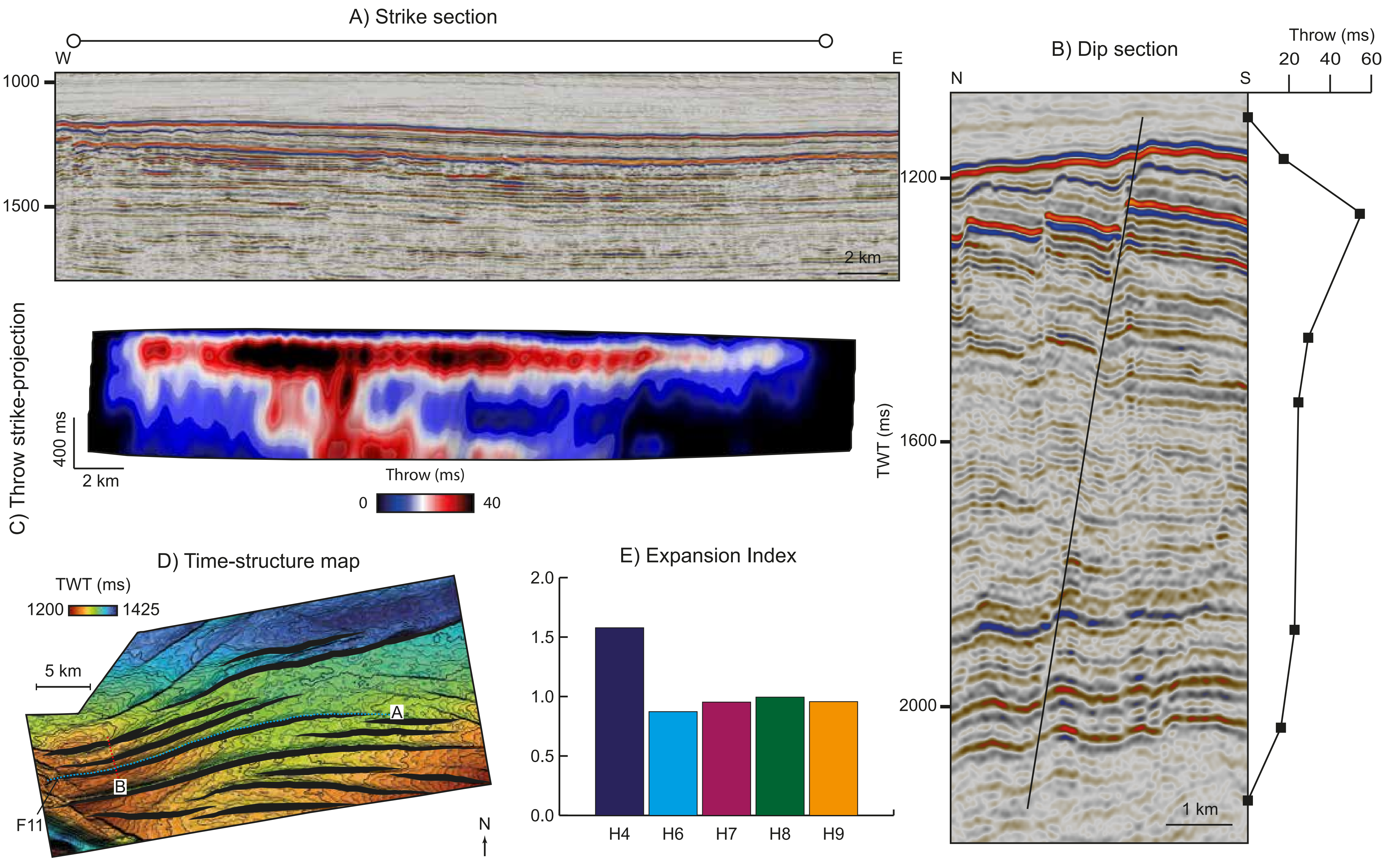

Fault 13 summary

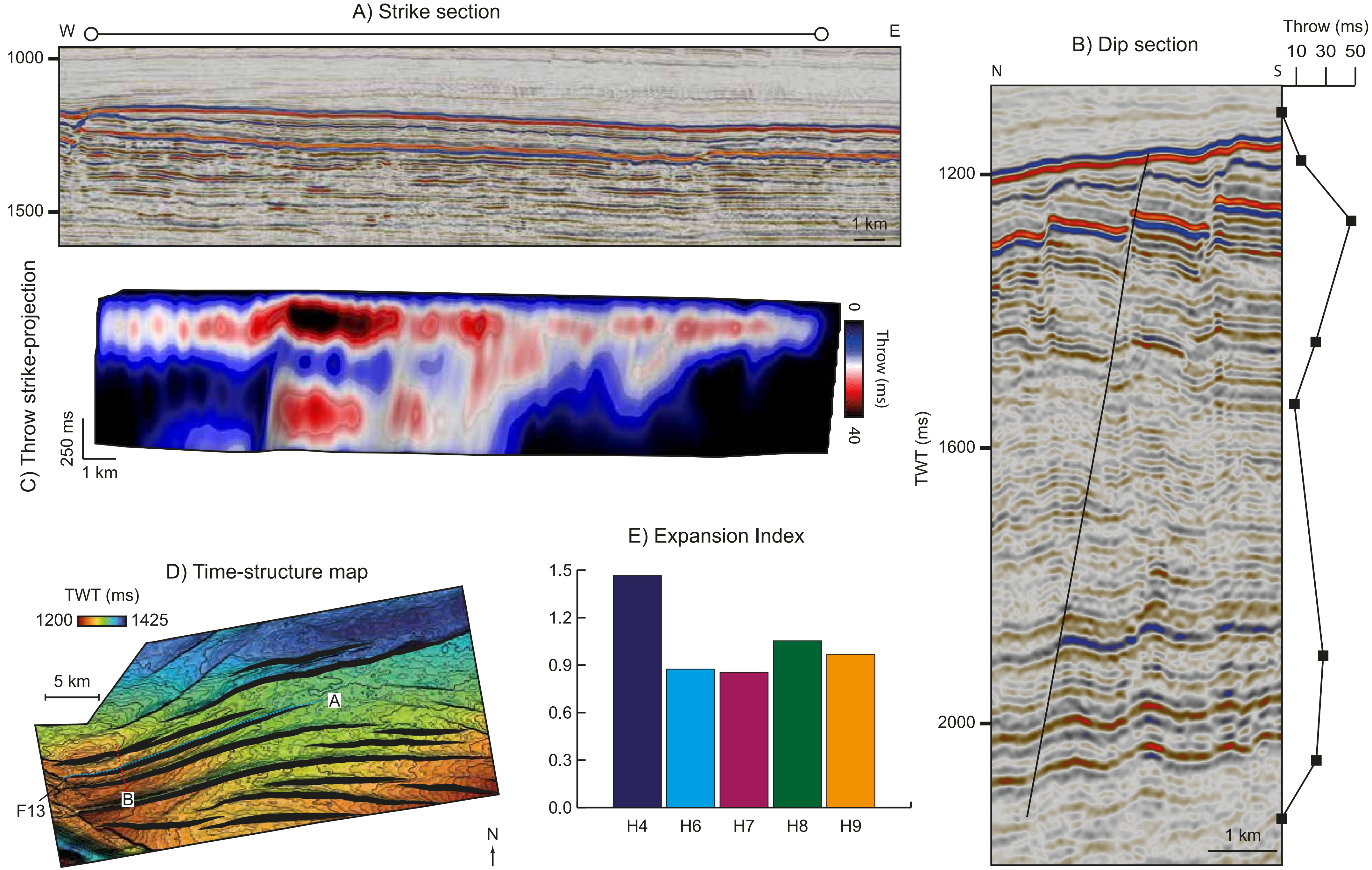

Fault 15 summary

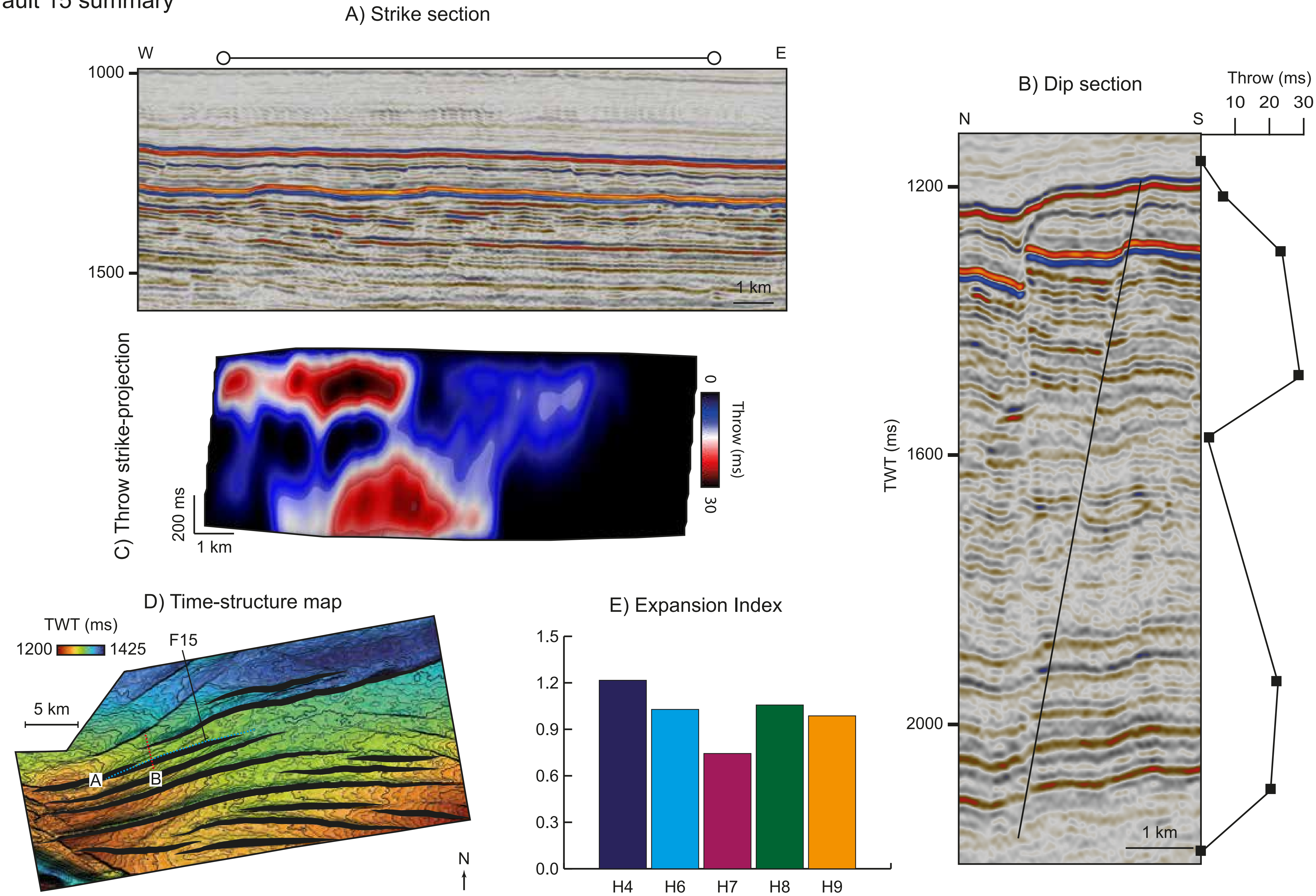

Fault 16 summary

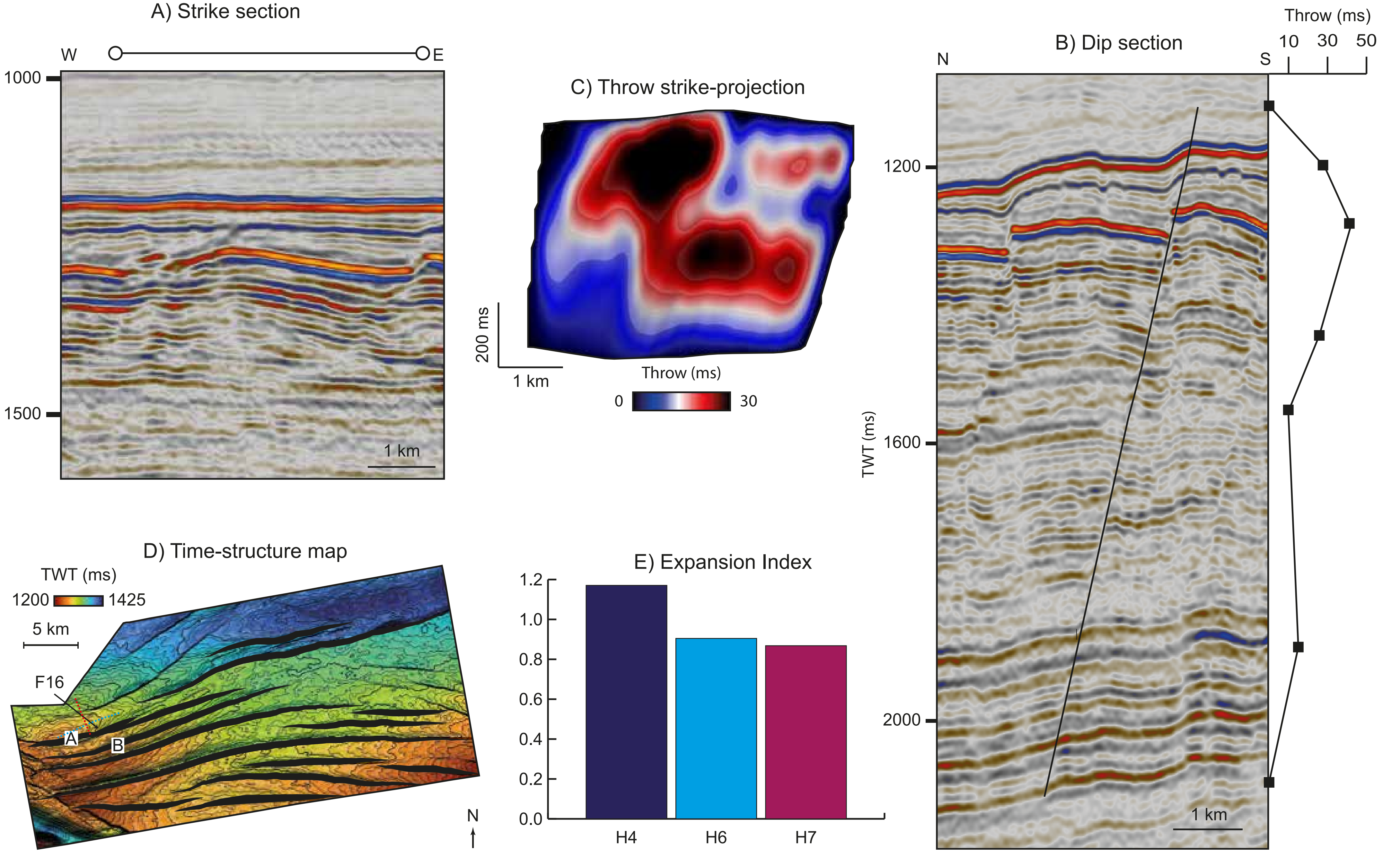

Fault 17 summary

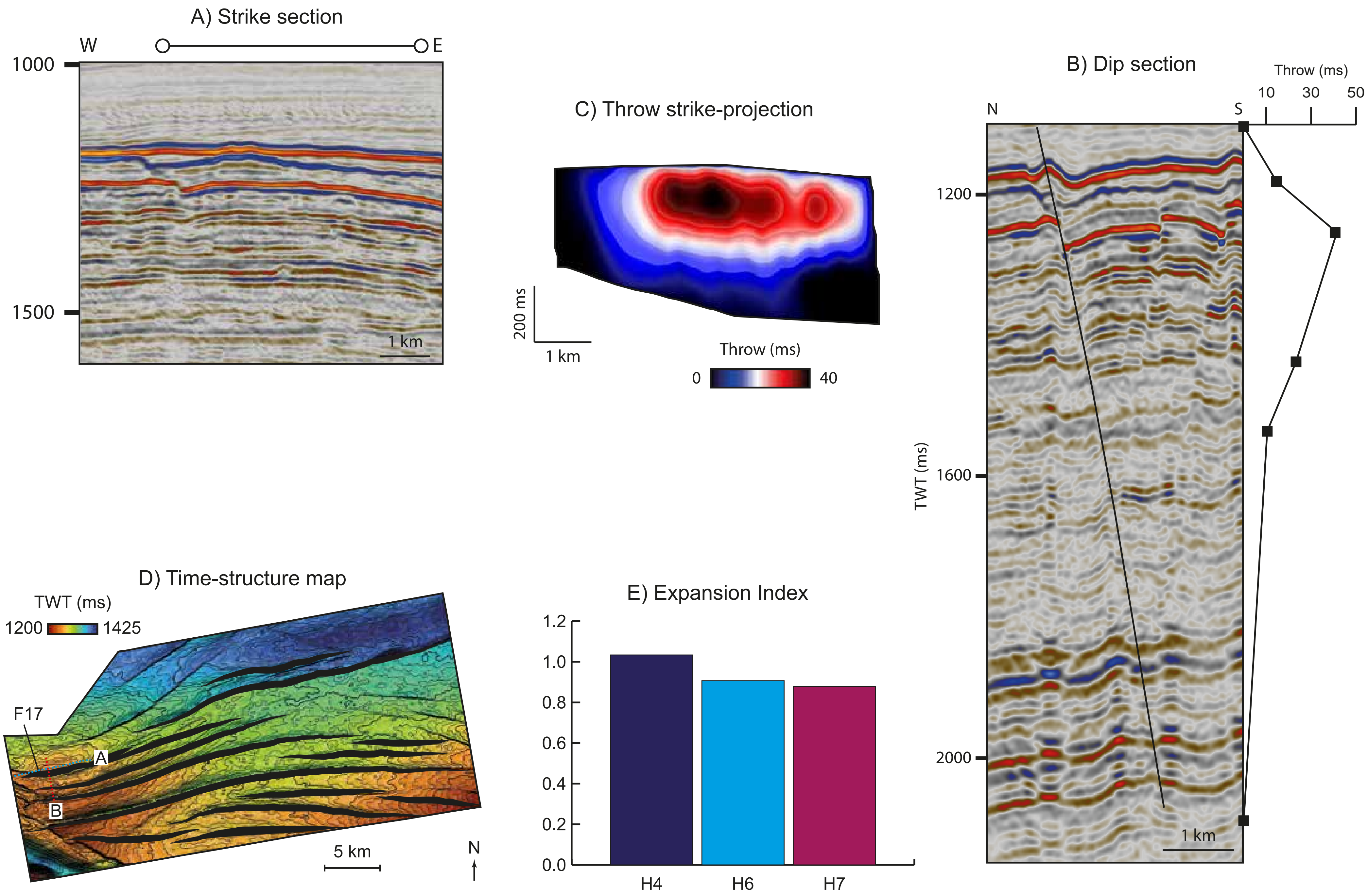

Fault 19 summary

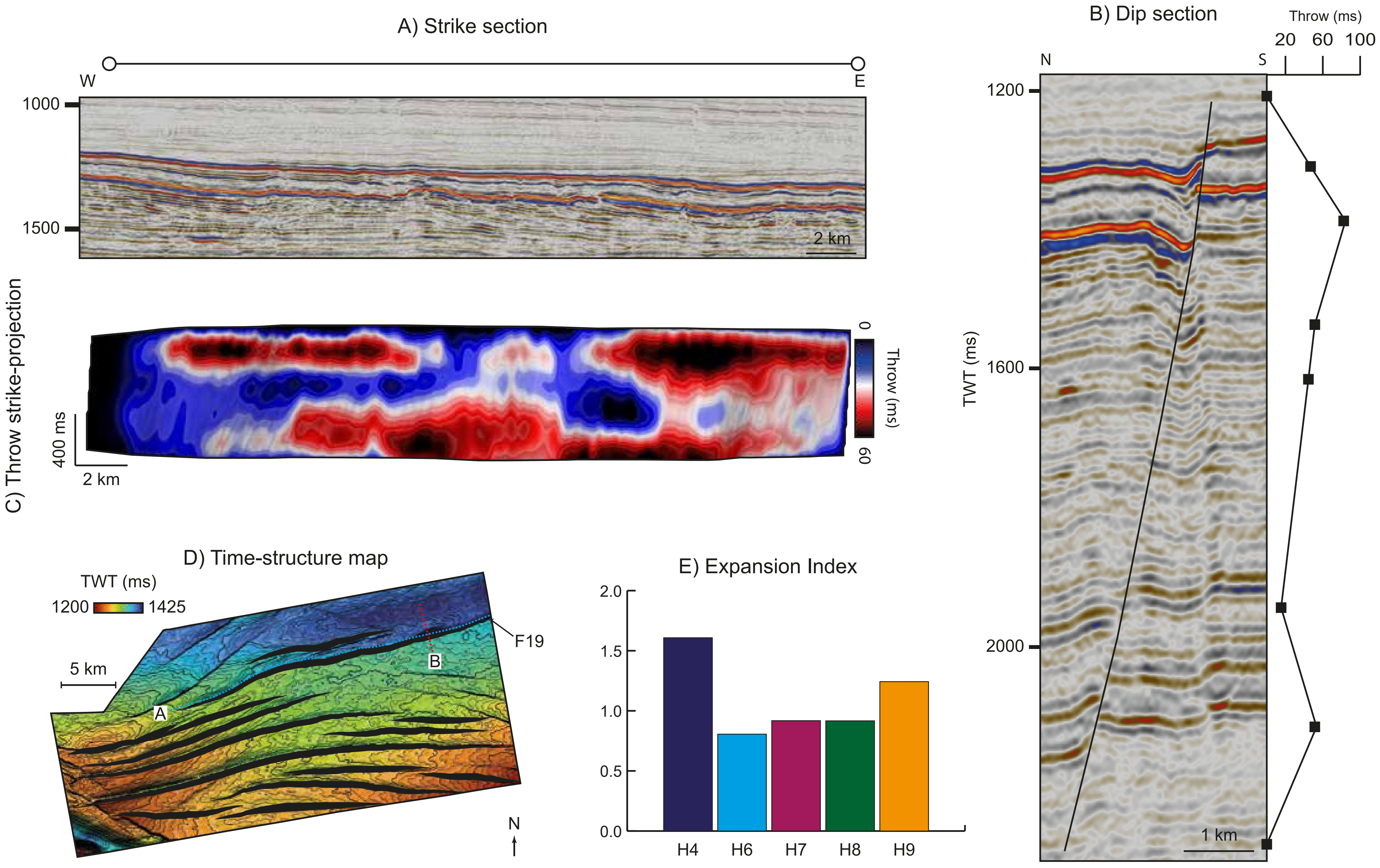

Fault 21 summary